Generation and Modeling of Alternating Magnetic Field in Undulator using Bulk High-Temperature Superconductor with Staggered Array Configuration

Ryota KINJO

Abstract

Aiming to contribute growth in synchrotron radiation based science by developing a short-period, high-field undulator for future storage rings or free-electron lasers, new undulator using bulk high-temperature superconductors with a staggered-array configuration in solenoid has been proposed and its magnetic properties were studied. First, the magnetic fields inside this undulator were theoretically analyzed by using a two dimensional physical model based on Bean's critical state model and two dimensional approximation. The analytical calculation shows the degree of dependence of these fields on the undulator parameters, the generation of a high undulator field proportional to the critical current density of the bulk superconductor, and the good tunability of the undulator field over a wide range of values. Second, experiment were performed using a six-periods prototype with the undulator period of 10 mm and the gap of 4 mm in a 2-T solenoid. The undulator field which has practical strength amplitude, 0.85 T at 20 K, and has wide tunability by the solenoid field were successfully demonstrated. The results also showed stronger undulator field can be generated by using stronger solenoid. The numerical calculation is performed in a three-dimensional geometry by two methods: the center field and energy minimization methods. The latter treats the current distribution inside the bulk, whereas the former neglects it as a natural extension of the analytical model. The calculation also reveals the dependence of the fields on the undulator parameters arising from the current distribution. From the comparison with experimental results, we find that the latter method reproduces the experimental

results well, which indicates the importance of the current distribution inside the bulk. Therefore, we derive a semi-empirical formula for the required solenoid field by modifying the analytical formula using the numerical results so as to include the effect of the current distribution. The semi-empirical formula reproduces the numerical result with an error of 3%. Finally, we estimate the magnetic performance of the undulator as an example of using the formulae and values presented in this thesis. The estimation shows that an undulator field twice as large as that of the present in-vacuum undulator but with an equal period and gap can be obtained at a temperature of approximately 20–40 K, and that deflection parameters (K values) of 1 and 2 can be achieved with periods of 5 and 10 mm at approximately 4–20 K.

Contents

Chapter 1

Introduction

Synchrotron radiation (SR) from a relativistic electron beam passing through a magnetic field is crucial to a wide range of scientific applications. Particularly, SR is important as a bright light source for X-ray science, for example, X-ray crystallography, X-ray absorption fine structure analysis, and X-ray fluorescence analysis. Undulator radiation, a SR from a relativistic electron beam passing through a periodic magnetic field in an undulator, is much bright, quasi-monochromatic, and wavelength-tunable light. Free electron laser (FEL), a SR from a microstructured electron beam due to interaction between the undulator radiation and the electron beam in an undulator, is also much bright wavelength-tunable laser. FEL is currently the only way to achieve practical lasers in X-ray region.

The fundamental wavelength of the undulator radiation and the FEL depends on the electron beam energy E, undulator period λ_u, and undulator field strength B_0. As undulators had typically had periods of around several centimeters, the only way to obtain bright undulator radiation in the hard X-ray region (10–25 keV) had been to use high-energy electron beams in large synchrotron facilities such as the European Synchrotron Radiation Facility in France (E = 6 GeV), Advanced Photon Source in the US (7 GeV), and SPring-8 in Japan (8 GeV). The demonstration of 4.6 keV X-ray gener-

ation from the 2.584 GeV synchrotron in the National Synchrotron Light Source was performed with an short-period, 11-mm-period, undulator [1]. Since then, moderate-energy synchrotron facilities with short-period undulators, such as the Swiss Light Source in Switzerland (E = 2.4 GeV, λ_u = 17 mm), DIAMOND in the UK (3 GeV, 21 mm), and SOLEIL in France (2.75 GeV, 20 mm), have been constructed [2, 3, 4]. In these facilities, undulator radiation harmonics from the 5th through 11th have been used to obtain 10–25 keV.

This scheme also prevails for FELs. The first X-ray laser of 0.12 nm (10 keV) was achieved at LCLS in the US (15 GeV, 30 mm) [5], and such lasers have already been used for X-ray science [6]. Subsequently, a 0.06 nm (20 keV) FEL has been achieved at SACLA in Japan (8 GeV, 18 mm) [7]. Recently, an X-ray FEL using the 3rd and 5th harmonics from a 3 GeV electron beam source and a 15-mm-period undulator has been proposed [8].

As can be concluded from the above, short-period undulators relax the requirement of the electron beam energy that means a lower operation and construction costs, an easier construction, and also opens opportunities for scientists to use hard X-rays in various applications. The undulator field strength, although not a determining parameter for wavelength, however must be sufficiently high to keep the radiation brilliance, particularly that of the harmonics, and the gain of amplification in FEL at high level with the short-period undulator and low-energy electron beam. In addition, the use of multi-MeV gamma rays from high-field, short-period undulators to generate polarized positron beams via particle-antiparticle pair production in future linear colliders has been proposed [9].

To realize a higher-field, shorter-period undulators, several different types of undulator have been studied. In-vacuum undulators (IVUs) [10], which have specially coated permanent magnet (PM) arrays inside a vacuum vessel, have been used in the aforementioned demonstration, in moderate-energy facilities, and in SACLA. Cryo-

genic PM undulators (CPMUs) [11], in which the residual flux and coercivity of PMs are enhanced by cooling the magnets in an IVU to 100–150 K, have been developed and put in use. An undulator using a low-temperature superconductor (LTS) wires in a vacuum vessel have been proposed and demonstrated by Hezel et al. [12], who attempted to remove the thick thermal insulation wall between the electron beam trajectory and the LTS wire.

Recently, bulk high-temperature superconductors (HTSs) have been extensively studied; a trapped field of over 17 T was reported in a 26-mm-diameter, 15-mm-thick bulk HTS at 29 K [13]. An undulator using a bulk HTS has several advantages over other undulators: (1) a bulk HTS can produce fields over 10 times stronger than those of PMs even when cooled; (2) the magnetic properties of bulk HTSs are continuing to improve whereas those of PM have been disputed; (3) HTSs are more suitable in high-current accelerators than LTSs because the thermal input from the electron beam and the radiation itself exceeds the refrigerator capacity at liquid helium temperatures; and (4) assembly is easier than for an undulator using an LTS wire. However, to use bulk HTSs in undulators, one has to investigate methods of magnetizing bulk HTSs and generating a sinusoidal magnetic field, i.e., undulator field. So far, various approaches to achieving this have been proposed. Cryoundulator plus (CU+) [14], in which bulk HTS rings are mounted on PMs to enhance the magnetic field in a CPMU, has been proposed and demonstrated. A superconducting permanent magnet undulator (SCPMU) [15, 16], in which bulk HTSs are magnetized by a dipole field perpendicular to the beam axis, has also been proposed and demonstrated.

At Institute of Advanced Energy, Kyoto University, bulk high-temperature superconductor staggered array undulator (BHSAU) is proposed [17]. In the BHSAU, bulk HTSs are magnetized by the solenoid field parallel to the beam axis. The advantage of the BHSAU over other types of the undulator using bulk HTSs are as follows: (1) Because the BHSAU use the bulk HTSs as main magnets, the higher field can be expected

if we used the bulk HTS with higher critical current density, while the performance in CU+ is limited by the performance of the PM; (2) Because of the field strength and the area of uniform field of a dipole magnet are in a trade-off relationship, the SCPMU has a limitation in its periodic number or the intensity of the magnetization. However, the BHSAU does not have such problem, because the field strength and the length of a solenoid are independent of each other. (3) The BHSAU is based on a conventional staggered-array undulator (SAU) [18], in which soft magnetic blocks are in staggered-array configuration instead of bulk HTSs. Therefore, as with the SAU, the undulator field of the BHSAU is expected to be controllable by the solenoid field, while the other undulators need the mechanical structure to control the gap of the magnet.

However, there are many physical and technical issues about the BHSAU. There is no analytical or numerical model of the BHSAU because of the difficulty of calculating magnetization of the bulk HTSs in the BHSAU. The current distribution inside a bulk HTS, which determine magnetization of the bulk HTS, depend on the field applied to the bulk HTS generated by solenoid and other bulk HTSs in the BHSAU. In other words, the magnetizations of bulk HTS are affected each other. Thus, the undulator field of the BHSAU can not be estimated. The dependence of the undulator field on the geometrical parameter is also not clear. The analytical or numerical model which treat field-dependent-magnetization of the bulk HTSs in the BHSAU is required. The experiment is required to prove the principle and to validate the analytical or numerical model.

In this thesis, the BHSAU is studied by the following analytical, experimental, and numerical ways

1. to prove the principle, i.e., the generation of the undulator field, and the controllability of the undulator field by the solenoid field

2. to find out the dependency of the undulator field on the geometrical parameters, the critical current density of the bulk HTS, and the solenoid field

3. to prove the high undulator field generation with short-period.

The details of the thesis are as follows.

In chapter 2, the basics of the synchrotron radiation, undulator radiation, and FEL are reviewed. Also reviewed are the basics of the bulk HTS and its magnetization process. Then, the history of undulators are reviewed in the view point of the development history of short-period, high-field undulators. Finally, the concept of BHSAU are described.

In chapter 3, the analytical model of the BHSAU are proposed based on the two-dimensional approximation and Bean's critical state model for hard type-II superconductor [19]; and the analytical formulae of the field inside the BHSAU are derived from the model by using the two-dimensional Biot-Savart's law. The characteristics of the BHSAU, i.e. the degree of dependence of the fields on the geometrical parameters, the applied solenoid field, and the critical current density of the bulk HTS, are presented and discussed.

In chapter 4, results of the prototype experiment are presented and discussed to prove the generation of a high undulator field and its controllability. The prototype has the periodic number of 6, the period of 10 mm, the gap of 4 mm, a 2-Tesla superconducting solenoid, and a cooling system by helium gas. The experimental results are also used to be compared with the numerical results in chapter 6 for their validation.

In chapter 5, a three-dimensional numerical model of the BHSAU is proposed based on Bean's critical state model. The two methods named center field (CF) method and energy minimization (EM) method are used to determine the current distribution in the numerical model. The former derives a simple current distribution as a natural extension of the analytical model to three-dimensional geometry. The latter derives the current distribution that varies in the z-direction inside each bulk HTS so that the magnetic energy is minimized. The numerical code based on the model and methods is developed. The differences in the results by two methods are presented, and the

importance of treating the current density is discussed. Also shown are newly revealed properties of the BHSAU which are not obvious in the analytical study.

In chapter 6, the comparisons of the analytical, experimental, and numerical results are performed. To evaluate the numerical model, how to make the comparison without the exact value of the critical current density in the experiment is investigated. The comparison results are presented and discussed. Next, to obtain formulae which include the factor of the current distribution, the semi-empirical formula for the required solenoid field is derived by modifying the analytical formula using the comparison results of the analytical and numerical calculations. Finally, the performance estimation of the BHSAU are shown by using the formulae to reveals out its possibility for application in the future.

Summary is given in chapter 7.

Chapter 2

Bulk High-Temperature Superconductor Staggered Array Undulator (BHSAU)

2.1 Introduction

In this chapter, the reason why we study the BHSAU is shown. First, the requirement of the short-period, high-field undulators are explained on the basis of the theories of SR, undulator radiation, and FELs. Second, the basic theory of the bulk HTS and its magnetization process is explained. Third, the development history of the short-period, high-field undulators is introduced. Finally, the principle of the BHSAU is described.

2.2 Theories of Radiation

2.2.1 Synchrotron Radiation

Synchrotron radiation (SR) is electromagnetic wave emitted from charged particles, especially electron beam with a relativistic speed, when they deflected by a magnetic force. SR is obtained from the bending magnets, which generates dipole magnetic field perpendicular to the electron beam trajectory, in electron storage rings. Generally, SR is much brighter than other light source in a wide range of the wavelength from infrared to hard X-ray, and thus largely used in a wide range of scientific applications. Particularly, SR is important as a bright light source for X-ray science, for example, X-ray crystallography, X-ray absorption fine structure analysis, and X-ray fluorescence analysis.

2.2.2 Undulator and Undulator Radiation

Figure 2.1 shows the concept of planar undulator. Usually, the coordinate of the system is taken as in the figure. The z-axis is matched to the direction of the electron beam. The y-axis is matched to the direction of the undulator field. The x-axis is matched to the diffraction direction of the electron beam by the undulator field. In the undulator, undulator field, a periodic magnetic field, is generated by upper and lower array of the magnets which have the periodic structure. Undulator radiation is one of SR from relativistic electron beam passing throughout the undulator field. However, by the interference effect of the light emitted at each period, undulator radiation is brighter than SR from the bending magnet and quasi-monochromatic. The undulator radiation is wavelength-tunable; the wavelength of the radiation can be varied by changing the electron beam energy or the strength of the magnetic field.

There are several types of undulator field which determine a trajectory of the electron beam and a polarization of the emitted radiation. Here, we describe a planar un-

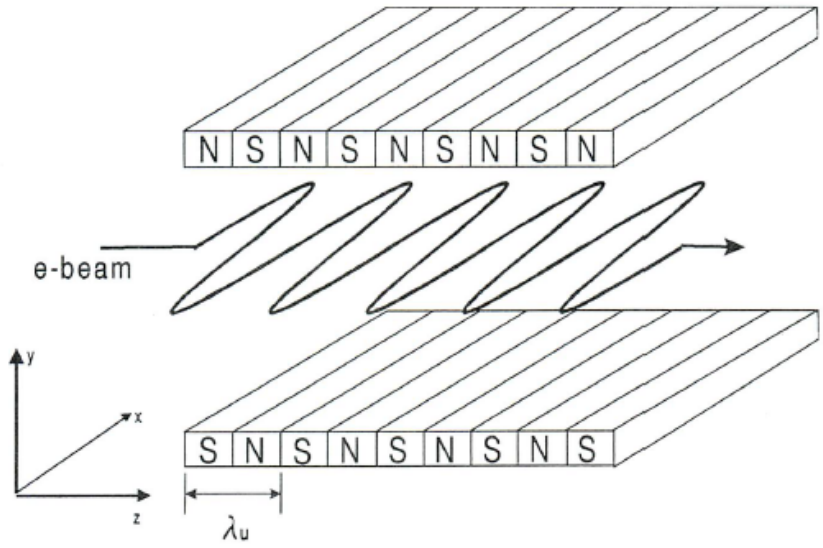

Figure 2.1: Concept of planar undulator [20]. The trajectory of the relativistic electron is wiggled in the xz plane by the periodic magnetic field in y-direction. The electron emit the radiations at each period and the radiations from each period interfere each other.

dulator which has a periodically alternating magnetic field approximately equal to a sinusoidal function. The fundamental wavelength of the undulator radiation λ_R is expressed by

$$\lambda_R = \frac{\lambda_u}{2\gamma}\left(1 + \frac{K^2}{2}\right). \tag{2.1}$$

Here, γ is the Lorentz factor of the electron beam, λ_u is the period of the undulator, and K is the diffraction parameter. The Lorentz factor means the relative electron beam energy and is defined by

$$\gamma = \frac{1}{\sqrt{(1-\beta^2)}}. \tag{2.2}$$

Here, β is the speed of electrons divided by the speed of light, v/c. The diffraction parameter K is usually called K value and is an important parameter which express the

strength of the undulator field and also the electron beam trajectory. It is defined as

$$K = \frac{eB_0\lambda_u}{2\pi m_e c}. \tag{2.3}$$

Here, e is the electron charge, B_0 is the undulator field, m_e is the electron mass, and c is the speed of light. Generally, γ and λ_u are fixed in the devices, K is adjusted by changing B_0 for changing the wavelength of the undulator radiation. To change B_0, the gap of the upper and lower magnets is changed. In practical units, it is written by

$$K \sim 93.37 B_0[\mathrm{T}]\lambda_u[\mathrm{m}]. \tag{2.4}$$

The total power of the undulator radiation P_T is expressed by

$$P_T \propto (2N-1)\lambda_u \gamma^2 B_0^2 I_b. \tag{2.5}$$

Here, N is the periodic number of the undulator, I_b is the electron beam current.

If λ_u become smaller, smaller λ_R can be obtained with the same γ, or the same λ_R can be obtained with the smaller γ. This means that if the undulator period is shorter, the short wavelength radiation, i.e, high energy photons, can be obtained in the existing electron storage rings, or new small storage ring with the lower electron beam energy can generate the same wavelength radiation as the existing large storage rings with the higher electron beam energy. The latter is especially important because the storage ring with the lower electron beam energy means lower costs, a shorter construction time, and less effort but would also provide opportunities for scientists to use hard X-rays in various applications. However, the total flux P_T become small when λ_u and γ is small. To keep the total flux high, B_0 must be high. Therefore, the short-period, high-field undulator is required. The history that the middle-energy storage rings with the short-period, high-field undulators come to the forefront is as already stated in Chap. 1. For practical purpose, the K value should be kept at approximately 0.5–2. For example, from the Formula 2.4, $B_0 > 1$ T is required for the undulator with $\lambda_u = 10$ mm to achieve $K = 1$, and $B_0 > 2$ T is required for the undulator with $\lambda_u = 5$ mm to achieve $K = 1$.

2.2.3 Free Electron Laser

In FEL, the undulator radiation is amplified by the interaction between the electron beam and the radiation in the undulator field [21]. The gain of the amplification is written by

$$G \propto \lambda_u^2 N^3 K^2 \gamma^{-3}. \tag{2.6}$$

The wavelength of FEL is written by the same formula for that of the undulator radiation. Here also, to obtain the same wavelength FEL but with the lower electron beam energy, the short-period undulator can be used. However then again, to keep the gain constant, large K is required. The gain is high when K is at approximately 1–2. Therefore, B_0 required for FEL is as same as that for the undulator radiation.

2.3 Theory of Bulk High-Temperature Superconductor and Its Magnetization

2.3.1 Superconductor

Type-I superconductor shows the perfect diamagnetism (Meissner-Ochsenfeld effect) below the critical field H_c and lose its superconductivity above H_c. Type-II superconductor does not lose its superconductivity even above the lower critical field H_{c1} and lose it above H_{c2}. From H_{c1} to H_{c2}, the superconducting and normal conducting states are coexistent, and then the magnetic field can enter into the superconductor. By adding the nano-particles which does not show superconductivity into the superconductor, the magnetic field can strongly be trapped at the normal conducting part. Then, the high current can flow without the energy loss due to the moving of the magnetic field. The important parameters of the superconductor is the critical temperature T_c, the critical current density J_c, and the critical field H_c (H_{c1}, H_{c2}). J_c largely depends on the

temperature of the superconductor, T, and exponentially decrease when T is close to T_c. Also, J_c decreases depending on the magnetic field applied to the superconductor, B. The degree of the decrease is depend on T; it is large at high T and small at low T; there is the effect named "peak effect" by which J_c has maximum at certain B. The dependence of J_c on B at various T, i.e., J_c–B curves, for the superconductor we use in the experiment is shown in Chap. 4. As shown in the figure, the dependence on the magnetic field is much smaller than that on the temperature.

The high-temperature superconductor (HTS) is a part of the type-II superconductor which has high T_c. Bulk HTS is bulk of that and used as PM by having the superconducting loop current inside it. A trapped field of over 17 T was reported in a 26-mm-diameter, 15-mm-thick bulk HTS at 29 K [13]. This is over 10 times larger than the surface magnetic flux of PMs. The material of bulk HTS is improving day by day. The manufacturing of bulk HTSs is also improved; the high quality bulk HTS with the diameter of over 130 mm can be created.

2.3.2 Bean's Critical State Model for Hard Type II Superconductor

Here, the process of magnetizing the bulk HTS is described on the basis of Bean's critical state model for hard type-II superconductors [19]. The critical state model is proposed by Bean. It states that the critical current density of the bulk HTS is determined so that the Lorentz force of the current on magnetic flux balances with the pinning force. Particularly the critical state model which assume the constant critical current density J_c independent on the magnetic field is called Bean's critical state model. The field dependent critical current density is treated in Kim model [22] or Irie-Yamafuji model [23]. The treatment of the critical current density in each model is

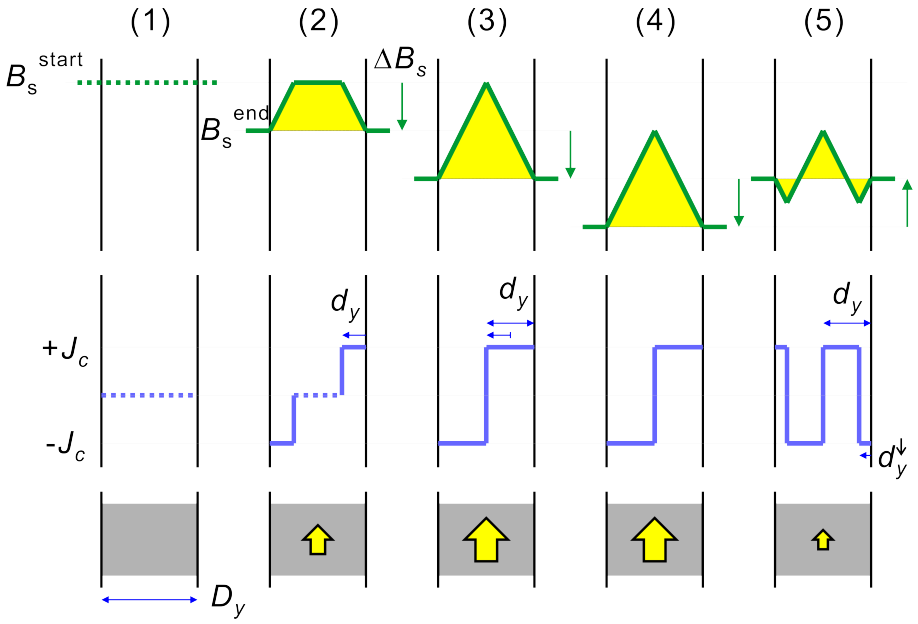

Figure 2.2: Principle of magnetization in infinite plane slab bulk HTS. The upper, middle, and lower figures shows the magnetic field, the current distribution, and the magnetization inside/outside the bulk HTS, respectively. By chaning the applied magnetic field, the current and the magnetization is induced in the bulk HTS.

written as

$$\begin{aligned} J_c(T) &= J_c(T), && \text{(Bean)} \\ J_c(T,B) &= \frac{\alpha_K(T)}{|B| + B_K(T)}, && \text{(Kim)} \\ J_c(T,B) &= \alpha_I(T)|B|^{\gamma_I(T)-1}. && \text{(Irie} - \text{Yamafuji)} \end{aligned} \tag{2.7}$$

Here, α_K, B_K, α_I, γ_I are the parameters to reproduce the experimental J_c–B curves. Bean's critical state model is quite clear and thus used in the explanation of the process of magnetization of the type-II superconductor. In this study, Bean's model is used.

Figure 2.2 shows the current and magnetic field distributions inside the bulk HTS. The bulk HTS has infinite plane with the thickness D_y. Part (1) and (2)–(5) show before

and after the magnetization, respectively. The top and middle parts show the magnetic field distribution and the current distribution in the cross-sectional plane of bulk HTS. The bottom part show the magnetization in the bulk HTS. Before the magnetization, the solenoid field of $B_s^{\rm start}$ is applied on the bulk HTS. Then, the bulk HTS is cooled below to the T_c. After that, the solenoid field is changed from $B_s^{\rm start}$ to $B_s^{\rm end}$. Then the loop current flows to negate the change of the magnetic field inside bulk HTS and does not decay because it is a supercurrent. Therefore, the bulk HTS works as PM. From the assumption in Bean's critical state model, the current density is equal to constant J_c at everywhere; and the current flow from the outer edge of the bulk HTS with the depth d_y. Using the changes of the solenoid field $\Delta B_s (= B_s^{\rm end} - B_s^{\rm start})$, d_y is written as

$$d_y = \begin{cases} \dfrac{\Delta B_s}{\mu_0 J_c} & \left(\Delta B_s \leq \dfrac{\mu_0 J_c B_{\rm max}}{2} \right) \\ \dfrac{D_y}{2} & \left(\Delta B_s > \dfrac{\mu_0 J_c B_{\rm max}}{2} \right) \end{cases}. \tag{2.8}$$

Here, μ_0 is the space permeability. The magnetization of the bulk HTS is determined from J_c and d_y. In Bean's critical state model, because field independent J_c is assumed, the magnetization of bulk HTS depends on ΔB_s not on the absolute value of B_s. The case of $B_s^{start} = 0$ T is called zero field cooling (ZFC) and the case of non-zero B_s^{start} is called field cooling (FC). In Chap. 4, the results of ZFC and FC are compared to reveal the effect of field-dependent J_c.

Individual differences in the critical current density among the bulk HTSs are briefly discussed. Figure 2.3 shows the magnetic field, the current density, and the magnetization of the bulk HTSs with high and low J_c at unsaturated and saturated region. At unsaturated region, the depth $d_y^{\rm L}$ in the bulk HTS with low J_c, $J_{\rm c}^{\rm L}$ is larger than the depth $d_y^{\rm H}$ in the bulk HTS with high J_c, $J_{\rm c}^{\rm H}$. Then, the relation

$$\Delta B_s = \mu_0 J_{\rm c}^{\rm L} d_y^{\rm L} = \mu_0 J_{\rm c}^{\rm H} d_y^{\rm H} \tag{2.9}$$

is true in the unsaturated region. The total amounts of the current are equal for both bulk HTSs. Thus, the magnetizations of bulk HTSs are almost the same in the region.

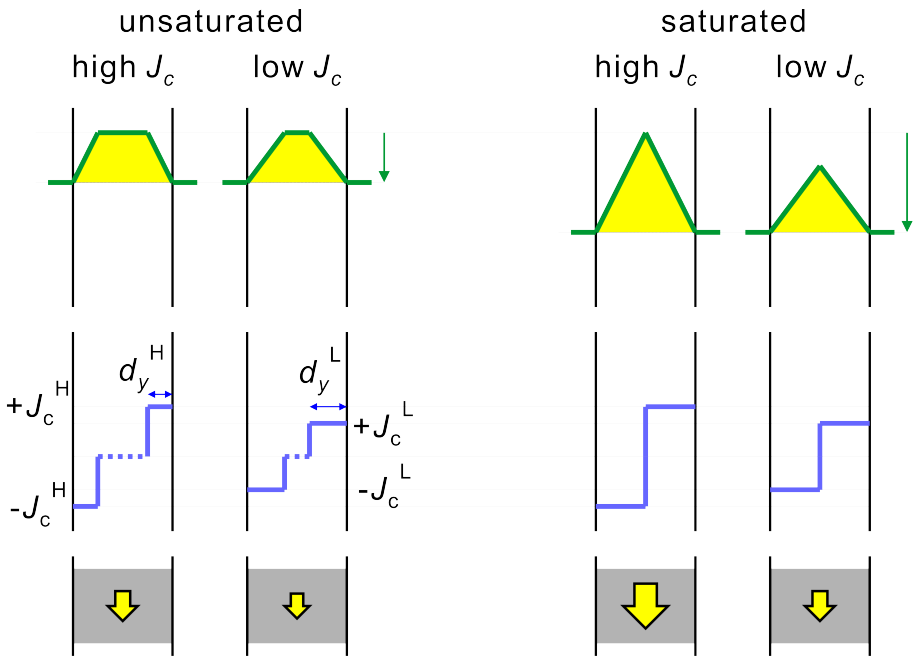

Figure 2.3: Difference of magnetization of high and low J_c bulk HTS. There is a small difference of the magnetizations in the unsaturated region whereas a large difference in the saturated region.

Whereas, for the unsaturated region, the relation is not true. The magnetizations of bulk HTSs are different depending on J_c. These fact connect to the error of the undulator field in BHSAU. The individual differences have little enfluence on the undulator field in the unsaturated region. On another front, the undulator field show errors in their amptides and phases depending on the individual difference in the saturated region. In this thesis, the experiment is performed only in the unsaturated region, and the individual differences are not taken into the calculation. It is because the individual differences of J_c of bulk HTSs used in the experiment are measured only at 77 K and not at the low temperature. Then, we only introduces that these phenomena were observed in the experiment at 77 K [24]. In the reference, the coefficient of variations (CV) for the peaks of the undulator field and that for J_c are compared. CV for peaks of the undulator

field was calculated using seven peaks around the center of BHSAU. CV for J_c of bulk HTSs was calculated using each trapped field profile of the stand alone bulk HTS. The experimental and numerical results showed that the former is smaller than third part of the latter at a point where the undulator field is the half of its saturated value. As will be noted in Chapter 5, the numerical code in this study can be applied to the future study for the dependency of the errors in the undulator field on the individual differences.

2.4 Development History of Short-Period, High-Field Undulators

Here, the history of undulators is introduced in the view point of the development history of the short-period, high-field undulators.

The concept of the undulator was proposed by Motz for a high-power source of microwave [25]. The undulator which generates light first was made of air core LTS coils [26]. The first undulator for electron storage ring was also made of LTS coils and magnetic yokes [27]. In this thesis, all of undulators using LTS are simply called superconducting undulator (SCU). And then, the undulator with PMs (PMU) were invented [28]. Generally, LTS coils can generate the larger field than PMs. However, because the gap of magnets in SCU were larger than that in PMU due to thick thermal shields between the electron beam trajectory and the LTSs, the undulator fields of SCUs were lower than that of PMUs. Therefore, PMU have been largely used worldwide.

In-vacuum undulators (IVUs) [10], which have specially coated PM arrays inside a vacuum vessel were invented at High Energy Accelerator Research Organization (KEK) and extensively introduced at SPring-8. The gap of magnets in a conventional PMU has a minimum limit because the vacuum duct is exists between the magnets. However, there is no limitation of the gap in an IVU because its magnets are inside a vacuum duct. The IVU has been a standard of a short-period, high-field undulator. As

mentioned in the Introduction, the 11-mm-period IVU was used in a demonstration of 4.6 keV X-ray generation from the 2.584 GeV synchrotron in the National Synchrotron Light Source [1]. IVU was installed to Swiss Light Source in Switzerland (E = 2.4 GeV, λ_u = 17 mm) [2] and largely used. Since then, moderate-energy synchrotron facilities such as DIAMOND in the UK (3 GeV, 21 mm), and SOLEIL in France (2.75 GeV, 20 mm), have been constructed [3, 4]. These facilities included the use of the IVUs from their design stages.

An undulator using LTS wires in a vacuum vessel, superconducting in-vacuum undulator (SIVU), have been proposed and demonstrated by Hezel et al. [12], who attempted to remove the thick thermal insulation wall between the electron beam trajectory and the LTS wire. However, it is not clear that the gap of SIVU can be small like IVU. It is because the main problem of the undulator using LTS is remained, i.e., the difficulty of keeping the LTS temperature below at about helium temperature under the large thermal input from the electron beam and the radiation.

Cryogenic PM undulators (CPMUs) [11], in which the residual flux and coercivity of PMs are enhanced by cooling the magnets in an IVU to 100–150 K, have been developed and put in use. The CPMU is thought to be the promising candidate of the next short-period, high-field undulator of the IVU.

The undulators using bulk HTS are proposed by Tanaka et al. Cryoundulator plus (CU+) [14], in which bulk HTS rings are mounted on PMs to enhance the magnetic field in a CPMU, has been proposed and demonstrated. A superconducting permanent magnet undulator (SCPMU) [15, 16], in which bulk HTSs are magnetized by a dipole field perpendicular to the beam axis, has also been proposed and demonstrated.

Staggered array undulator (SAU), in which soft magnetic blocks are in staggered-array configuration, was proposed by Ho et al. [18]. The soft magnetic blocks are magnetized in the z-direction by the solenoid aligned so that the central axis of the undulator coincided with that of the solenoid; the staggered-array configuration of the

blocks make the magnets generate the undulator field. The SAU has several advantages over PMUs. (1) Because the SAU consists of only the soft magnetic blocks and non-magnetic pieces like coppers to support the soft magnet block, the SAU is easy to construction. (2) Because of the same reason as (1), the SAU is relatively resistant to the thermal and the radiation damage. Thus, gap of SAU can be smaller than PMUs. (3) The undulator field of the SAU can be controlled by the solenoid field. Thus, the large base which open or close the gap of undulator is not required. At Institute of Advanced Energy, Kyoto University, the compact infrared FEL, Kyoto University Free Electron Laser (KU-FEL) has been developed for energy related sciences. At KU-FEL facility, the magnetic properties of the SAU as a compact undulator has been studied [29]. Also at KU-FEL facility, T. Kii et al. proposed a SAU like undulator using Meissner effect of superconductor [30]. Using perfect diamagnetic blocks instead of soft magnetic blocks in SAU can also generate the undulator field. Although this idea did not work well [31] because the perfect diamagnetic property is broken much lower field than practical level, these studies on SAU continues to the idea of BHSAU.

In this section, the history of the undulator were reviewed in the view point of the development history of the short-period, high-field undulators. Addition to the benefit of the short-period, high-field undulators to the large light source facility mentioned in Introduction, here the benefit to small FEL facility is briefly introduced. At the KU-FEL facility, the electron beam of up to 10 MeV is generated by a thermionic RF gun, and accelerated to 25–40 MeV by a traveling-wave accelerating tube. The undulator period is 33 mm. The target wavelength is 5–20 μm. If undulator with the period of 5 mm is used instead of the present undulator, the required electron beam energy for the target wavelength can be reduced to around 10 MeV. This means that the accelerating tube, the second klystron for that, and the concrete shield for neutrons which generated by the high-energy electrons can be removed. Thus, KU-FEL can be a more compact IR FEL facility.

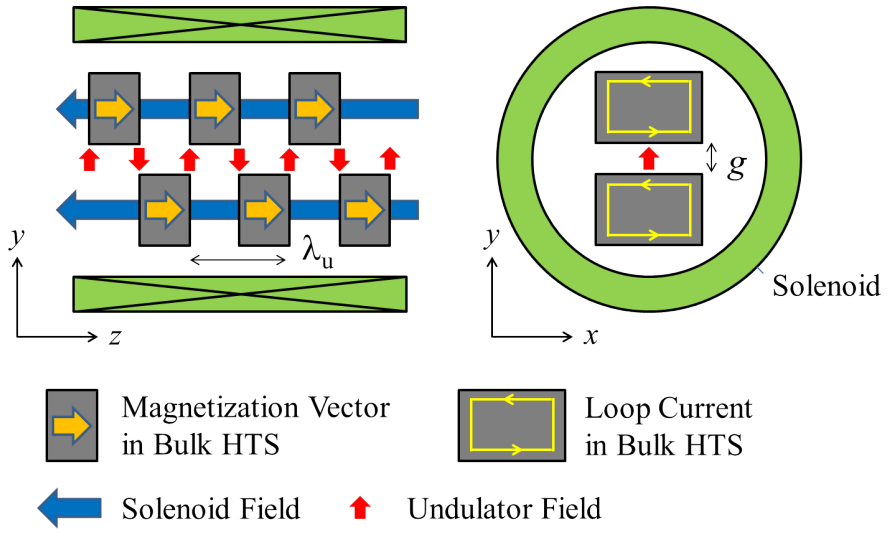

Figure 2.4: Schematic view of BHSAU. The change of the solenoid field in z-direction induces the superconducting loop currents inside the bulk HTSs. The loop currents generates the periodic field in y-direction.

2.5 Bulk High-Temperature Superconductor Staggered Array Undulator

At Institute of Advanced Energy, Kyoto University, bulk HTS staggered array undulator (BHSAU) was proposed.[17]. A schematic diagram of the BHSAU is shown in Fig. 2.4. The green blocks indicate a solenoid and the blue arrows indicate the solenoid field. The gray blocks indicate bulk HTSs. The orange arrows and the yellow loop indicate the magnetization and the loop current generated by the change in the solenoid field inside bulk HTSs, respectively. The red arrows indicate the undulator field generated by the bulk HTSs.

The principle of operation is as follows. When a negative-z-direction solenoid field is applied to the bulk HTSs, superconducting current loops are established to negate the change in the magnetic field inside the bulk HTSs; therefore, the bulk HTSs obtain positive-z-direction magnetization and thus generate a sinusoidal magnetic field in the

y-direction. The BHSAU is based on a conventional SAU, therefore, the BHSAU inherits the properties of an SAU, i.e., tunability of the undulator field by the solenoid field. The advantages of the BHSAU are as follows. Because the undulator field is generated by bulk HTSs, which are magnetized in the same direction, one external solenoid can magnetize all the bulk HTSs and control the undulator field by controlling the magnetization of the bulk HTSs. Thus, a mechanical structure to control the gap is not required. Considering the large attraction force in a high-field undulator and the fact that cracking of the bulk HTSs occurred in the demonstration experiment of CU+, this is a major advantage.

Chapter 3

Analytical Calculation of BHSAU

3.1 Introduction

Analytical formulation of undulator field and a study based on the formula are important works to estimate the performance of undulators. Until now, however, no analytical study of BHSAU has been performed. In this chapter, we perform an analytical study to check roughly the basic characteristic of BHSAU. The more precise calculation and the comparison with the experimental result are performed with the numerical results later. Here, we clarify the undulator field generation and its controlling by the solenoid field. We also clarify the rough approximation of the amplitude of the undulator field and the dependence of these on the parameters. In section 3.2, we make the two dimensional model of BHSAU based on Bean's critical state model of type-II superconductor [19]; then we derive the analytical formulation of the undulator field by using the two-dimensional form of Biot-Savart's law. In section 3.3, we show dependence of the undulator field on the undulator parameters, the critical current density, and the applied solenoid field. In section 3.4, the results are discussed. In the calculation, we mainly use our prototype parameters as representatives value (λ_u = 10 mm, g = 4 mm).

3.2 Method

3.2.1 Two-dimensional Analytical Model of BHSAU

We calculate the magnetic field generated by infinitely long coils which represents bulk HTSs placed regularly as shown in Fig. 3.1. Here, λ_u is the period of the undulator, g is the gap of the upper and the lower magnet arrays, D_z and D_y are respectively z and y dimension of the bulk HTS, d_y is the depth of the shielding current inside the bulk HTS, and the points P (0, $g/2 + D_y/2$) and Q ($\lambda_u/2$, 0) are used in the following calculation. The geometry is as follows.

1. The coils are infinitely-long in x-direction.

2. The model has infinite period in z-direction.

3. The coils are placed with the period of λ_u. There is the difference of $\lambda_u/2$ in z-direction between the upper and the lower coils.

We obtained this model by assuming the following.

1. Because undulator has large enough periodic number (typically from several tens of to a few hundreds of periods), infinite period in z-direction in z-direction is assumed.

2. The size of bulk HTS in x-direction is much larger than the period ($D_x >> \lambda_u$). Thus, the coils are assumed infinitely long in x-direction.

3. The depth of the shielding current d_y is not a function of z. Figure 3.2 shows the current distribution inside the bulk HTS in two dimension. The magnetic field is applied from the right to the left. The left part shows the well-known current distributions in (a) a finite-thickness bulk HTS standing alone and (b) an infinite-thickness bulk HTS. The right part shows the assumed current distribution in

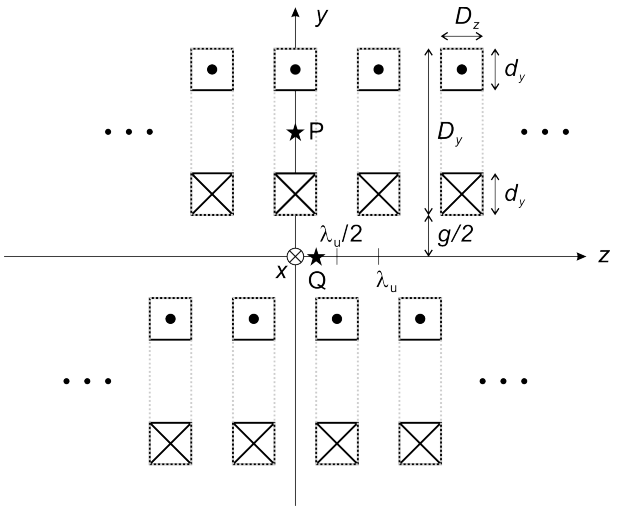

Figure 3.1: Two-dimensional current coil model of BHSAU. The dotted box indicates the place of bulk HTS which has the dimensions of $D_z \times D_y$, however, only the $\pm x$-direction currents in vacuum space is considered in the model. The point P and Q are the observer point of the field.

(c) finite-thickness bulk HTSs stacked infinitely. For simplicity, we assumed the uniform current density in (c). In chapter 5, the numerical calculation treats the current distribution which vary with the z-direction position; the comparison with the numerical result is discussed in chapter 6.

4. Bean's critical state model assume that the current density inside the superconductor is the same with the critical current density, J_c^{bulk}, or zero; the critical current density is constant everywhere independent on the magnetic field. Therefore, we assume that all coils have the same current density equal to J_c^{bulk}.

From the assumptions 4, all coils have the same current:

$$I = J_c^{\mathrm{bulk}} D_z d_y. \tag{3.1}$$

Because the loop current flows to negate the change of the solenoid field, we assume that B_z generated by the loop current in the center of the bulk is the same with

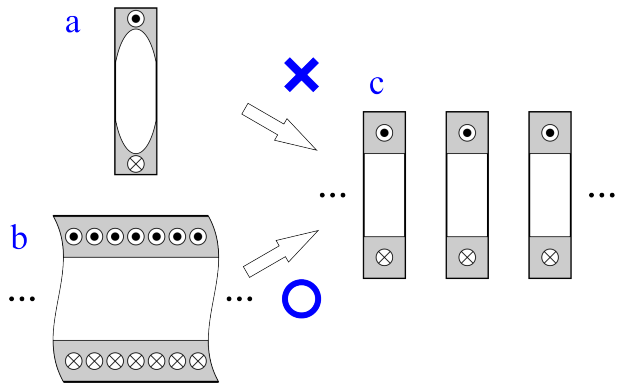

Figure 3.2: Current distribution inside the bulk HTS in two dimension. The magnetic field is applied from the right to the left. The left part shows the well-known current distribution in (a) a finite-thickness bulk HTS standing alone and (b) an infinite-thickness bulk HTS. The right part shows the assumed current distribution in (c) finite-thickness bulk HTSs stacked infinitely. For the simplicity of the model, the distribution in a single bulk HTS (a) is neglected.

the solenoid field change $-\Delta B_s$. In the following calculation, for the convenience of the calculation, ΔB_s is calculated from B_z at point P by using the given parameters including d_y:

$$\Delta B_s \equiv -B_z(\mathrm{P}). \tag{3.2}$$

The amplitude of the undulator field B_0 is obtained by the formula:

$$B_0 \equiv |B_y(\mathrm{Q})|\,. \tag{3.3}$$

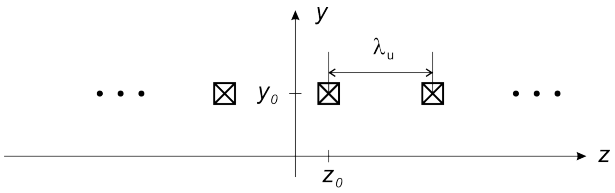

Figure 3.3: Single line of current coils

3.2.2 Analytical Formulae for Undulator Field and Required Solenoid Field

Formulation

Let us calculate the magnetic field in the model. First, we consider a single line of current coils on the equal y-position as shown in Fig. 3.3. We consider the case when $D_z \to 0$ and $d_y \to 0$ with the current I inside the coil being kept constant. The current density in such coils is expressed as

$$j(\xi = z + \mathrm{i}y) = I\delta(y - y_0) \sum_{n=-\infty}^{\infty} \delta(z - z_0 - n\lambda_u). \tag{3.4}$$

Because $j(\xi)$ is periodic along the z-axis, it can be expanded into a Fourier series,

$$j(\xi = z + \mathrm{i}y) = I\delta(y - y_0) \left\{ \frac{1}{\lambda_u} + \frac{2}{\lambda_u} \sum_{n=1}^{\infty} \cos \frac{2n\pi}{\lambda_u}(z - z_0) \right\}. \tag{3.5}$$

If we put one coil on the origin ($z_0 = 0$ and $y_0 = 0$), we have

$$j(\xi = z + \mathrm{i}y) = I\delta(y) \left\{ \frac{1}{\lambda_u} + \frac{2}{\lambda_u} \sum_{n=1}^{\infty} \cos \frac{2n\pi}{\lambda_u} z \right\}. \tag{3.6}$$

The magnetic field generated in the yz plane is expressed by the two-dimensional form of Biot-Savart's law,

$$b^* = b_z - \mathrm{i}b_y = -\frac{\mu_0}{2\pi\mathrm{i}} \int \frac{j(\xi')}{\xi - \xi'} \mathrm{d}\xi'. \tag{3.7}$$

By substituting Eq. (A.1) into Eq. (3.7), we have

$$b^* = -\frac{\mu_0}{2\pi\mathrm{i}} \frac{I}{\lambda_u} \int_{-\infty}^{\infty} \frac{1 + 2\sum_{n=1}^{\infty} \cos \frac{2n\pi}{\lambda_u} z'}{z' - \xi} \mathrm{d}z'. \tag{3.8}$$

By executing the integration the formula (see Appendix), we obtain

$$b_z = \mathrm{sgn}(y)\frac{\mu_0 I}{2\lambda_u}\left[1 + 2\sum_{n=1}^{\infty}\cos(\beta z)e^{-\beta|y|}\right], \tag{3.9}$$

$$b_y = -\frac{\mu_0 I}{\lambda_u}\sin(\beta z)e^{\beta|y|}. \tag{3.10}$$

By integrating the formula with the cross-sectional area of the coil ($D_z \times d_y$), we obtain the magnetic field generated by the coils:

$$\begin{aligned} B_z(z,y) &= \int_{-d_y/2}^{+d_y/2}\int_{-D_z/2}^{+D_z/2} b_z(z-z_0, y-y_0)\,\mathrm{d}z_0\,\mathrm{d}y_0 \\ B_y(z,y) &= \int_{-d_y/2}^{+d_y/2}\int_{-D_z/2}^{+D_z/2} b_y(z-z_0, y-y_0)\,\mathrm{d}z_0\,\mathrm{d}y_0 \\ &\qquad\qquad (y < -d_y/2, +d_y/2 < y). \end{aligned} \tag{3.11}$$

The total magnetic field is obtained by the superposition of 4 lines of coils. The magnetic field generated by the coils on the gap ($-g/2 < y < g/2$) is expressed as

$$\begin{aligned} B_y(z,y) = &-\mu_0 J_c^{\mathrm{bulk}}\lambda_u \sum_{n=1}^{\infty}\frac{\sin\left(nk_u D_z/2\right)\sin\left(nk_u z\right)}{n^2\pi^2} \\ &\times \cosh(nk_u y)\,\mathrm{e}^{-nk_u g/2}\left(1-\mathrm{e}^{-nk_u(D_y-d_y)}\right)\left(1-\mathrm{e}^{-nk_u d_y}\right) \\ &\qquad\qquad (-g/2 < y < g/2), \end{aligned} \tag{3.12}$$

$$\begin{aligned} B_z(z,y) = &-\mu_0 J_c^{\mathrm{bulk}}\lambda_u \sum_{n=1}^{\infty}\frac{\sin\left(nk_u D_z/2\right)\cos\left(nk_u z\right)}{n^2\pi^2} \\ &\times \sinh(nk_u y)\,\mathrm{e}^{-nk_u g/2}\left(1-\mathrm{e}^{-nk_u(D_y-d_y)}\right)\left(1-\mathrm{e}^{-nk_u d_y}\right) \\ &\qquad\qquad (-g/2 < y < g/2). \end{aligned} \tag{3.13}$$

Here, k_u is the wavenumber defined by $k_u = 2\pi/\lambda_u$.

The magnetic field generated by the coils at $y = g/2 + D_y/2$ is expressed as

$$B_y\left(z, \frac{g}{2}+\frac{D_y}{2}\right) = 0, \tag{3.14}$$

$$B_z\left(z, \frac{g}{2}+\frac{D_y}{2}\right) = \frac{\mu_0 J_c^{\text{bulk}}}{2}\left[d_y + T(z)\right], \tag{3.15}$$

$$T(z) = \lambda_u \sum_{n=1}^{\infty} \frac{\sin\left(nk_u D_z/2\right)\cos(nk_u z)}{n^2\pi^2}\left(1-\mathrm{e}^{-nk_u d_y}\right) \times \left\{2e^{-nk_u(D_y/2-d_y)} + e^{-nk_u(g+D_y/2)}\left[1-e^{-nk_u(D_y-d_y)}\right]\right\}.$$

Therefore, the undulator field B_0 and the required solenoid field change ΔB_s are expressed as

$$B_0 = \mu_0 J_c^{\text{bulk}} \lambda_u \sum_{n=1}^{\infty} \frac{\sin\left(nk_u D_z/2\right)}{n^2\pi^2} \times \mathrm{e}^{-nk_u g/2}\left(1-\mathrm{e}^{-nk_u(D_y-d_y)}\right)\left(1-\mathrm{e}^{-nk_u d_y}\right), \tag{3.16}$$

$$\Delta B_s = -\frac{\mu_0 J_c^{\text{bulk}}}{2}\left[d_y + T\right], \tag{3.17}$$

$$T = \lambda_u \sum_{n=1}^{\infty} \frac{\sin\left(nk_u D_z/2\right)}{n^2\pi^2}\left(1-\mathrm{e}^{-nk_u d_y}\right) \times \left\{2e^{-nk_u(D_y/2-d_y)} + e^{-nk_u(g+D_y/2)}\left[1-e^{-nk_u(D_y-d_y)}\right]\right\}.$$

The dependence of B_0 on ΔB_s can be plotted by using d_y as parameter.

Parameter Binding and Simplification

To make the following study easier, parameters D_z and D_y in Formulae (3.16) and (3.17) should be fixed.

First, let us fix the D_y. Because $e^{-nk_u(D_y-d_y)} < e^{-nk_u D_y/2}$ $(0 < d_y < D_y/2)$ and $e^{(-nk_u D_y/2)} \ll 1$ at $D_y = 2\lambda_u$, we get $e^{-nk_u(D_y-d_y)} \ll 1$ $(0 < d_y < D_y/2)$ at $D_y = 2\lambda_u$. Thus, $D_y = 2\lambda_u$ is used in the following [1] , and then we assume

[1] Although we decide D_y for convenience of the calculation, the condition $D_y = 2\lambda_u$ is not unrealistically large for short-period undulators which have λ_u of at most 20 mm. The high quality QMG-GdBCO crystal which has the diameter of 85 mm has been manufactured [32],

$1 - e^{-nk_u(D_y - d_y)} \to 1$.

Next, let us fix D_y at the value for the maximum B_0 under the fixed ΔB_s condition. First and second order total differential of B_0 by d_y and D_z are expressed as

$$\mathrm{d}B_0 = \frac{\partial B_0}{\partial d_y}\mathrm{d}d_y + \frac{\partial B_0}{\partial D_z}\mathrm{d}D_z, \tag{3.18}$$

$$\mathrm{d}^2B_0 = \frac{\partial^2 B_0}{\partial d_y^2}\mathrm{d}d_y^2 + 2\frac{\partial B_0}{\partial d_y}\frac{\partial B_0}{\partial D_z}\mathrm{d}d_y\mathrm{d}D_z + \frac{\partial^2 B_0}{\partial D_z^2}\mathrm{d}D_z^2. \tag{3.19}$$

And the first order total differential of ΔB_s by d_y and D_z is expressed as

$$\mathrm{d}\Delta B_s = \frac{\partial \Delta B_s}{\partial d_y}\mathrm{d}d_y + \frac{\partial \Delta B_s}{\partial D_z}\mathrm{d}D_z. \tag{3.20}$$

Because we fixed ΔB_s, by using $\mathrm{d}\Delta B_s = 0$, then we have

$$\frac{\mathrm{d}d_y}{\mathrm{d}D_z} = -\left(\frac{\partial \Delta B_s}{\partial d_y}\middle/\frac{\partial \Delta B_s}{\partial D_z}\right) \equiv -A. \tag{3.21}$$

By substituting this to Eq. (3.18) and (3.19), we have

$$\frac{\mathrm{d}B_0}{\mathrm{d}D_z} = -A\frac{\partial B_0}{\partial d_y} + \frac{\partial B_0}{\partial D_z}, \tag{3.22}$$

$$\frac{\mathrm{d}^2B_0}{\mathrm{d}D_z^2} = A^2\frac{\partial^2 B_0}{\partial d_y^2} - 2A\frac{\partial B_0}{\partial d_y}\frac{\partial B_0}{\partial D_z} + \frac{\partial^2 B_0}{\partial D_z^2}. \tag{3.23}$$

At $D_z = \lambda_u/2$, because $\partial\Delta B_s/\partial d_y = 0$ and $\partial\Delta B_s/\partial D_z \neq 0$, we found $A = 0$. Therefore, we have

$$\left.\frac{\mathrm{d}B_0}{\mathrm{d}D_z}\right|_{D_z=\lambda_u/2} = \left.\frac{\partial B_0}{\partial D_z}\right|_{D_z=\lambda_u/2} = 0, \tag{3.24}$$

$$\left.\frac{\mathrm{d}^2B_0}{\mathrm{d}D_z^2}\right|_{D_z=\lambda_u/2} = \left.\frac{\partial^2 B_0}{\partial D_z^2}\right|_{D_z=\lambda_u/2} < 0. \tag{3.25}$$

From this formula, B_0 takes the local maximum at $D_z = \lambda_u/2$ under the fixed ΔB_s condition. Therefore, we decided to use $D_z = \lambda_u/2$.

Substituting $D_y = 2\lambda_u$, $1 - e^{-nk_u(D_y - d_y)} \to 1$, and $D_z = \lambda_u/2$ into the Formula 3.16 and 3.17, we have

$$B_0 = \mu_0 J_c^{\mathrm{bulk}}\lambda_u \sum_{n=1,3,\cdots}^{\infty} \frac{\sin(n\pi/2)}{n^2\pi^2}\,\mathrm{e}^{-nk_u g/2}\left(1 - \mathrm{e}^{-nk_u d_y}\right), \tag{3.26}$$

$$\Delta B_s = -\frac{\mu_0 J_c^{\mathrm{bulk}}}{2} d_y. \tag{3.27}$$

Here, we also assume $T = 0$ because T/d_y is smaller than 10^{-3} in the range $0 \leq d_y \leq D_y/2$ and $0.1 \leq g/\lambda_u \leq 10$, These formulae are used in the calculations for the results section.

One can write B_0 as a explicit function of ΔB_s. By substituting the Formula (3.27) to the Formula (3.26), we have

$$B_0 = \mu_0 J_c^{\mathrm{bulk}} \lambda_u \sum_{n=1,3,\cdots}^{\infty} \frac{\sin(n\pi/2)}{n^2\pi^2} \exp\left(-\frac{nk_u g}{2}\right) \left[1 - \exp\left(\frac{-4n\pi\Delta B_s}{\mu_0 J_c^{\mathrm{bulk}} \lambda_u}\right)\right]. \tag{3.28}$$

Initial gradient of ΔB_s–B_0 curve

Let us derive the initial gradient of ΔB_s–B_0 curve,

$$\left.\frac{\mathrm{d}B_0}{\mathrm{d}\Delta B_s}\right|_{\Delta B_s = 0}, \tag{3.29}$$

which is useful to discuss the result without knowing the exact value of J_c^{bulk}. Differentiating B_0 with respect to d_y, we obtain

$$\frac{\mathrm{d}B_0}{\mathrm{d}d_y} = 2\mu_0 J_c^{\mathrm{bulk}} \sum_{n=1}^{\infty} \frac{\sin^2(n\pi/2)}{n\pi} \mathrm{e}^{-nk_u g/2} \mathrm{e}^{-nk_u d_y}. \tag{3.30}$$

Differentiating ΔB_s with respect to d_y, we obtain

$$\frac{\mathrm{d}\Delta B_s}{\mathrm{d}d_y} = \frac{\mu_0 J_c^{\mathrm{bulk}}}{2} \left[1 + 2\sum_{n=1}^{\infty} \frac{\sin(n\pi/2)}{n\pi} \mathrm{e}^{-nk_u d_y} \mathrm{e}^{-4n\pi} (2\,\mathrm{e}^{nk_u d_y} + \mathrm{e}^{-nk_u g})\right]. \tag{3.31}$$

Therefore, the gradient $\mathrm{d}B_0/\mathrm{d}\Delta B_s$ at $\Delta B_s = 0$ ($d_y = 0$) is expressed as

$$\begin{aligned} \left.\frac{\mathrm{d}B_0}{\mathrm{d}\Delta B_s}\right|_{\Delta B_s = 0} &= \left(\frac{\mathrm{d}B_0}{\mathrm{d}d_y} \Big/ \frac{\mathrm{d}\Delta B_s}{\mathrm{d}d_y}\right)_{d_y = 0} \\ &= 4\sum_{n=1}^{\infty} \frac{\sin^2(n\pi/2)}{n\pi} \mathrm{e}^{-nk_u g/2}. \end{aligned} \tag{3.32}$$

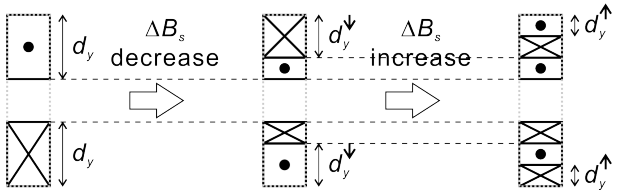

Figure 3.4: Depths of current flowing layers in single bulk HTS. The loop current starts to flow in the same or opposite direction depending on the change direction of the solenoid field. The loop current always starts to flow from the outer edge of the bulk HTS.

Formulae for B_0 control

Next, let us derive the formulae to calculate the control curve of B_0. The control curve means the ΔB_s–B_0 curve to control B_0 for wavelength tuning after once B_0 reached the target value of the operation. From Bean's critical state model, if we decrease ΔB_s from the target point, the current of the reverse direction starts to flow from the outer edge of the bulk. Define $d_y^{\downarrow}$ as the depth of the current flowing layer of the reverse direction current, then, the magnetic field is described by the superposition of the magnetic fields generated by the positive current (the depth is d_y) and by the negative current (the depth is $d_y^{\downarrow}$) :

$$B_0^{\downarrow}(J_c, d_y^{\downarrow}) = \begin{cases} B_0(J_c, d_y) - 2B_0(J_c, d_y^{\downarrow}) & (0 < d_y^{\downarrow} \leq d_y) \\ -B_0(J_c, d_y^{\downarrow}) & (d_y < d_y^{\downarrow} \leq D_y/2) \end{cases} . \tag{3.33}$$

The formula for $\Delta B_s^{\downarrow}(d_y^{\downarrow})$ is identical. If we increase ΔB_s again, the current which has the same direction with the original current starts to flow from the outer edge of the bulk. Define $d_y^{\uparrow}$ as the depth of the current flowing layer of the current, then, the magnetic field is described by the superposition of the magnetic fields generated by the

positive current (the depths are d_y and $d_y^{\uparrow}$) and by the negative current (the depth is $d_y^{\downarrow}$):

$$B_0^{\uparrow}(J_c, d_y^{\uparrow}) = \begin{cases} B_0^{\downarrow}(d_y^{\downarrow}) + 2B_0(J_c, d_y^{\uparrow}) & (0 \leq d_y^{\uparrow} \leq d_y^{\downarrow}) \\ B_0(J_c, d_y) & (d_y^{\downarrow} < d_y^{\uparrow} \leq d_y) \\ B_0(J_c, d_y^{\uparrow}) & (d_y < d_y^{\uparrow} \leq D_y/2) \end{cases} . \tag{3.34}$$

The formula for $\Delta B_s^{\uparrow}(d_y^{\uparrow})$ is identical.

3.3 Results

3.3.1 Undulator Field and Its Dependence on Structure Parameters

Formula (3.12) shows the following properties:

1. B_y is a sinusoidal function of z and the fundamental period is λ_u
2. B_y has odd harmonics (3rd, 5th, ...)
3. B_y is a hyperbolic cosine function of y
4. B_y has an exponential dependence on g/λ_u
5. B_y has a linear dependence on J_c^{bulk} and λ_u
6. B_y has a dependence on d_y/λ_u

Formula (3.13) shows that there is no B_z component generated by the coils on the z-axis.

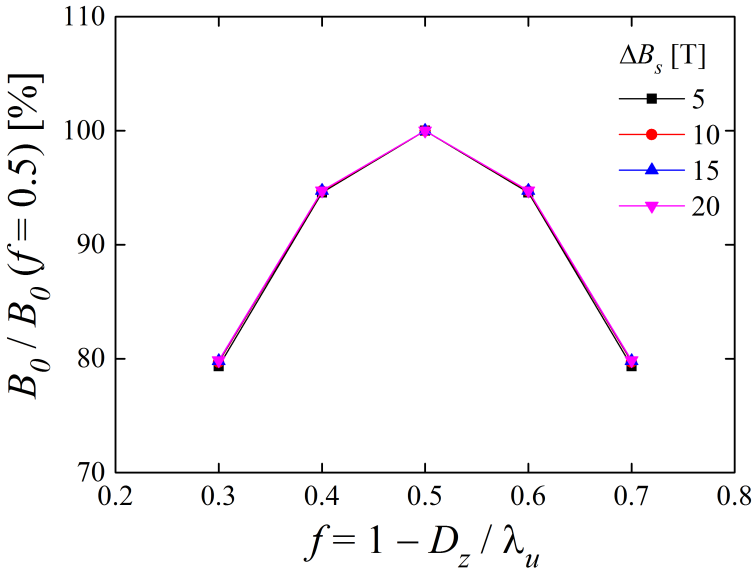

Figure 3.5: Dependence of B_0 on D_z at $J_c^{\mathrm{bulk}} = 5\ \mathrm{kA/mm^2}$ (λ_u = 10 mm, g = 4 mm)

3.3.2 Dependence on Thickness of Bulk HTS

Figure 3.5 shows dependence of B_0 on D_z at $\Delta B_s = 5, 10, 15, 20$ T. B_0 is normalized by B_0 at $f = 0.5$. Here, f is the parameter expressed by $f = 1 - D_z/\lambda_u$, indicating the ratio of vacant space to the period. As also shown in the expression (1.21) and (1.22), B_0 takes maximum at $f = 0.5$.

3.3.3 Theoretical Limits

Substituting $d_y = D_y/2 = \lambda_u$ into Eq. (3.26), we obtain the theoretical limit of B_0, $B_{0,\mathrm{max}}$ at the certain undulator parameters and J_c^{bulk}. Figure 3.6 shows the $B_{0,\mathrm{max}}$ dependence on λ_u and g at J_c^{bulk} = 10 kA/mm^2. The red, black, blue lines indicate the gap of 2, 4, 6 mm, respectively. The dotted and dashed lines indicate the required magnetic field to get $K = 1$ and 2, respectively.

Moreover, by substituting $d_y = D_y/2 = \lambda_u$ into Eq. (3.27), we obtain the ΔB_s

Table 3.1: Examples of maximum B_0 and ΔB_s

	λ_u [mm]	g [mm]	$B_{0,\max}/J_c$ [T/(kA/mm^2)]	$\Delta B_{s,\max}/J_c$ [T/(kA/mm^2)]
(a)	18	3.6	1.26	13.4
(b)	10	4	0.364	7.45
(c)	5	1	0.350	3.72

required to get $B_{0,\max}$, $\Delta B_{s,\max}$. As examples, $B_{0,\max}$ and $\Delta B_{s,\max}$ for the three representative parameters are shown in Table 3.1. In the table, $B_{0,\max}$ and $\Delta B_{s,\max}$ is normalized by $J_c^{\rm bulk}$, thus, one can get $B_{0,\max}$ by multiplying $J_c^{\rm bulk}$. The parameter set (a) is equal to the IVU in SACLA, (b) is equal to our experimental setup, (c) is equal to our target period.

If we take only $n = 1$ in Eq. (3.26), we can obtain the simple formula:

$$B_{0,\max} \sim 1.3 \times 10^{-2} J_c^{\rm bulk} \lambda_u \exp\left(-\pi \frac{g}{\lambda_u}\right) \tag{3.35}$$

where the units are $B_{0,\max}$ [T], $J_c^{\rm bulk}$ [kA/mm^2], λ_u [mm], and g [mm]. Substituting $d_y = D_y/2 = \lambda_u$ into Eq. (3.27), we obtain the required ΔB_s to get $B_{0,\max}$,

$$\Delta B_{s,\max} \sim 0.74\, J_c^{\rm bulk} \lambda_u. \tag{3.36}$$

For instance, substituting $J_c^{\rm bulk} = 10$ kA/mm^2, λ_u = 10 mm, $g = 4$ mm, we obtain $B_{0,\max} = 3.7$ T, $\Delta B_{s,\max} = 74$ T.

3.3.4 Dependence on Solenoid Field and Critical Current Density

Figure 3.7 shows the dependence of B_0 on ΔB_s at each $J_c^{\rm bulk}$ (λ_u = 10 mm, g = 4 mm). The lower figure is an enlarged view of the upper figure. B_0 increased with the increase in B_s with the similar shape of curves. As is clear from the fact that the both B_0 and ΔB_s are the linear function of $J_c^{\rm bulk}$, the curves are similar in shape and

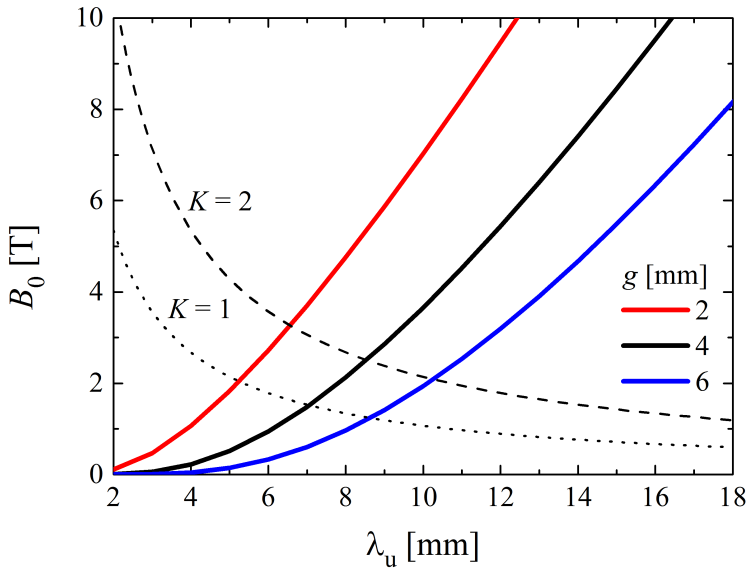

Figure 3.6: Dependence of maximum B_0 on λ_u and g at $J_c^{\mathrm{bulk}} = 10$ kA/mm^2. The dotted and dashed lines indicate the required field to achieve $K = 1$ and 2 at the period, respectively.

Table 3.2: Examples of operation B_0 at various ΔB_s. $B_0/B_{0,\max}$ is calculated at $g/\lambda_u = 0.4$, and has 2% accuracy around $0.1 \leq g/\lambda_u \leq 10$.

	Γ_y [%]	$B_0/B_{0,\max}$ [%]	$\Delta B_s/\Delta B_{s,\max}$ [%]
(a)	5	29	4.2
(b)	10	48	8.5
(c)	15	63	12.7
(d)	20	72	17.0
(e)	25	80	21.2
(f)	30	86	25.5
(g)	100	100	100

the maximum B_0 is proportional to $J_c^{\rm bulk}$. As is clear from the fact that $\mathrm{d}B_0/\mathrm{d}\Delta B_s$ at $\Delta B_s = 0$ depend not on $J_c^{\rm bulk}$ but on only the structure parameters, the curves have the equal gradient at $\Delta B_s = 0$.

In Fig. 3.8, $B_0/B_{0,\max}$ and $\Delta B_s/\Delta B_{s,\max}$ at $g/\lambda_u = 0.1, 10$ are shown. Here, $B_{0,\max}$ and $\Delta B_{s,\max}$ are the maximum B_0 and ΔB_s at $d_y = D_y/2 = \lambda_u$, respectively. There is only at most 3 percent difference between the curves at $g/\lambda_u = 0.1$ and $g/\lambda_u = 10$. The representative values in this graph is listed in Table 3.2. Here, the Γ_y is defined by $2d_y/D_y$. The index (a)–(g) will be referred in chapter 6. The values in the table was calculated with g/λ_u and matches the values at $0.1 < g/\lambda_u < 10$ with 2% inaccuracy. From the table, about the half of $B_{0,\max}$ can be obtained when only 8.5% of $\Delta B_{s,\max}$ is applied, or about 86% of $B_{0,\max}$ can be obtained when 25.5% of $\Delta B_{s,\max}$ is applied.

3.3.5 Controlling of Undulator Field by Solenoid Field

Figure 3.9 shows the dependence of B_0 on ΔB_s at λ_u = 10 mm and g = 4 mm. The upper figure shows the initial curves for various $J_c^{\rm bulk}$. The plot was obtained from

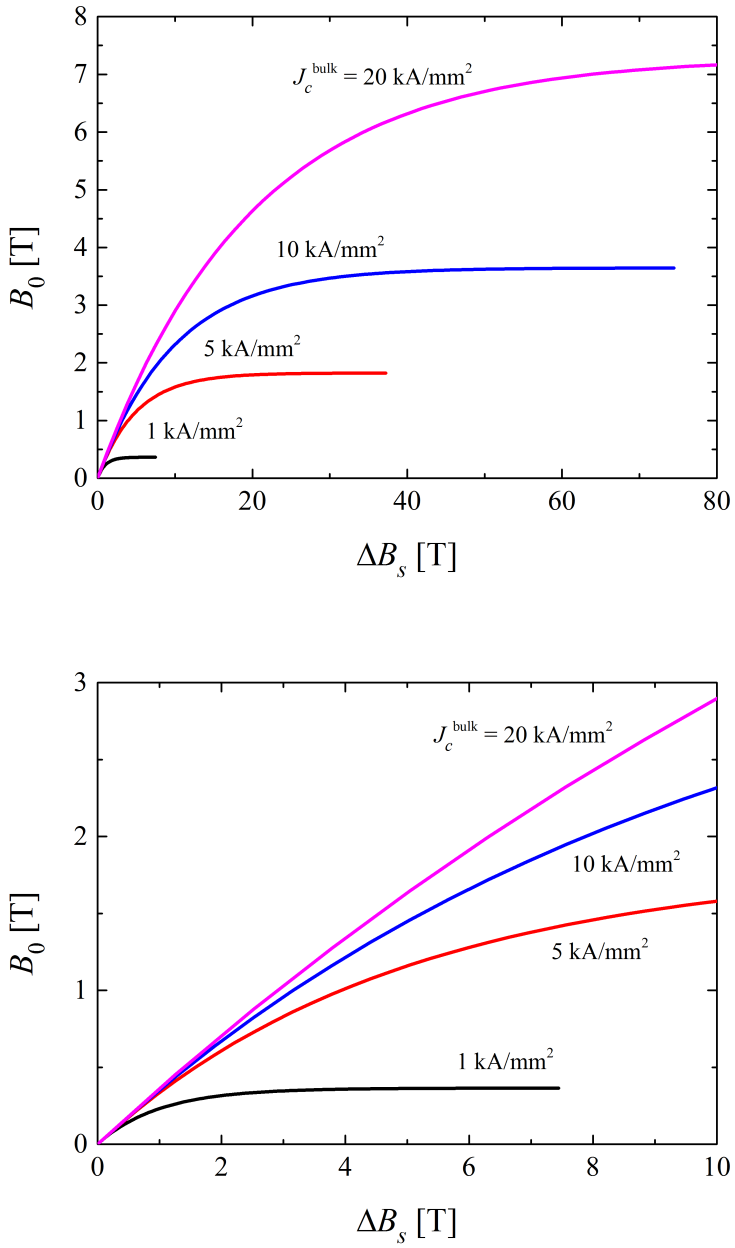

Figure 3.7: (UPPER) Dependence of B_0 on ΔB_s at each J_c^{bulk} (λ_u = 10 mm, g = 4 mm) and (LOWER) enlarged view.

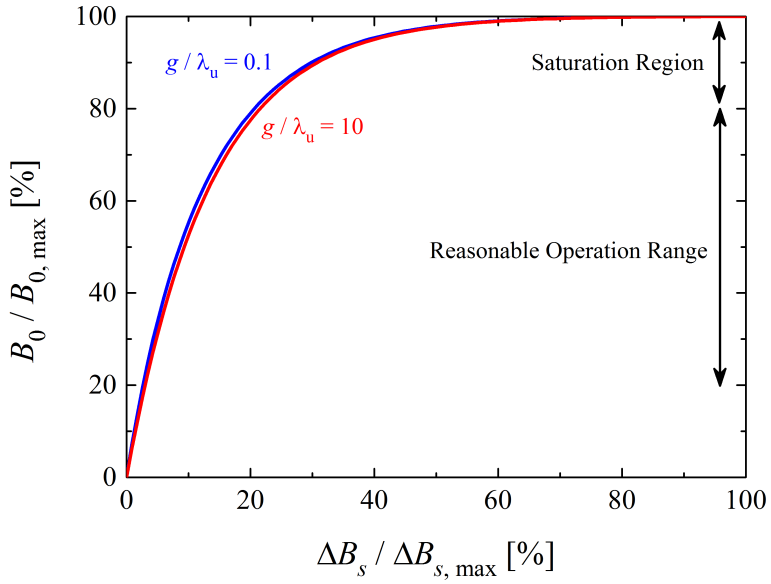

Figure 3.8: Dependence of B_0 on ΔB_s at $g/\lambda_u = 0.1, 10$.

Formulae (3.16) and (3.17) by using d_y as a parameter. The lower figure shows (1) the initial curve and sample control curves, i.e., (2) a curve to decrease B_0 and (3) a curve to increase B_0 again. The plot was obtained from Formulae (3.33) and (3.34) using d_y, $d_y^{\downarrow}$, and $d_y^{\uparrow}$ as parameters. Here, the initial curve is the curve when the bulk is magnetized after the superconducting transition, and the control curves are the curves used to tune the wavelength of the undulator radiation during operation. There was hysteresis in ΔB_s–B_0 curve.

3.4 Discussion

From the results of section 3.3.1, here we discuss the feature of the magnetic field in BHSAU. The field in PMU is expressed as

$$B_y = 2B_r \sum_{n=1,5,\ldots}^{\infty} \frac{\sin\left(\frac{n\pi}{4}\right)}{\frac{n\pi}{4}} \sin(nk_u z) \exp\left(-nk_u \frac{g}{2}\right) \left[1 - \exp\left(-nk_u H\right)\right] \qquad (3.37)$$

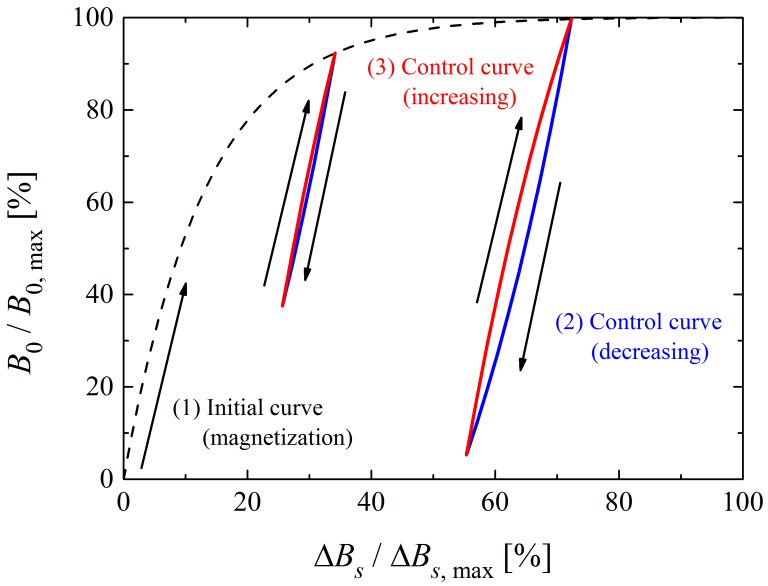

Figure 3.9: Dependence of B_0 on ΔB_s (Analytical, $\lambda_u = 10$ mm, $g = 4$ mm). The upper figure shows the initial curves at various J_c^{bulk}. The lower figure shows the initial curve and the samples of control curves.

where B_r is the remanent magnetic flux density of the permanent magnet and H is the height of the magnet in y-direction. Comparing the formula for BHSAU with that for conventional PMU, we found that the properties 1, 3, 4 in section 3.3.1 are also seen in PMU. The difference in field harmonics is originated from the geometric difference; PMU has 4 magnets per period in both sides. The 5th and 6th property are unique nature of BHSAU. The undulator field B_0 proportionally increases with increase of $J_c^{\rm bulk}$. The 6th property is one important feature for the field tunability of BHSAU.

From the results of section 3.3.2, we found that B_0 takes maximum at $f = 0.5$. This is a different feature from the conventional SAU. In a conventional SAU, because the distortion of the solenoid field is an origin of the undulator field, $f = 1 - D_z/\lambda_u < 0.5$ give the maximum undulator field [29]. To check f parameter dependence of the undulator field, z-direction distribution of the shielding-current depth in the bulk HTS should be considered in the chapter 5.

From the results in section 3.3.3, we found that the BHSAU can not be operated at the maximum especially for high $J_c^{\rm bulk}$ because the solenoid field required to generate the maximum B_0 is extremely high in commercial sense. In case of $J_c = 10$ kA/mm^2, the maximum field, $B_0 = 12.6$ T at $\lambda_u = 18$ mm and $g = 3.6$ mm, is about 10 times higher than that of IVU at the same λ_u and g. However, required solenoid field change, $\Delta B_s = 134$ T, can not be obtainable in commercial sense. Therefore, the results in section 3.3.4 is important. The undulator field, $B_0 = 3.7$ T at $J_c = 10$ kA, $\lambda_u = 18$ mm, and $g = 3.6$, can be obtained only with $\Delta B_s = 5.6$ T ($\Gamma_y = 5\%$), and is still about 3 times higher than that of IVU at the same λ_u and g. This solenoid field change can be obtained by the present superconducting magnet. Even if the required solenoid field change is obtainable in commercial sense, the operation in 'reasonable operation range' in Fig. 3.8 is more reasonable than that in 'saturation region' because of the following two reasons. One is the cost of the superconducting solenoid. The other is the effect of the high solenoid field (z-direction field) on the trajectory of the

electron beam. The electron trajectory will take a cyclotron motion in addition to the undulating motion, and then the properties of the radiation emitted from the electron beam changes. Detailed discussion on those is out of the scope of this study.

We found that the BHSAU has high undulator field with high J_c, however, the both $J_c^{\rm bulk}$ and Γ_y should be considered. For example, $B_0 = 1.1$ T at $\lambda_u = 10$ mm and $g = 4$ ($K = 1$) can be obtained with two different conditions: with $J_c = 10$ kA/mm^2 and $\Delta B_s = 3.1$ T ($\Gamma = 5\%$) and with $J_c = 6$ kA/mm^2 and $\Delta B_s = 3.8$ T ($\Gamma = 10\%$). In case of J_c =6 kA/mm^2, BHSAU can be operated in high temperature. To design the BHSAU effectively, the suitable $J_c^{\rm bulk}$ and Γ_y should be chosen for target B_0 and given boundary conditions. In the real machine, $J_c^{\rm bulk}$ is mainly determined by the operation temperature, and Γ_y is determined by the applied solenoid field change. Because the operation temperature and the required solenoid field change affects the required specification of the most costly parts, i.e., the cooling system and the superconducting solenoid, it is important to choose $J_c^{\rm bulk}$ and Γ_y properly.

From the results of section 3.3.5, we can say that the controllability of B_0, meaning the tunability of the radiation wavelength, is kept at good level even in the saturation region. The original SAU has almost no tunability in the saturation region in which the SAU has the high undulator field. BHSAU overcome this weakpoint of the original SAU.

3.5 Conclusion

This study is the first ever theoretical analysis of BHSAU. The most important conclusion of this study is that BHSAU has high undulator field and good tunability within reasonable solenoid field. The knowledge is used for the discussion of the numerical study and prototype experiments in the following part.

Chapter 4

Experiment

4.1 Introduction

In the previous chapter, we theoretically showed that by using the BHSAU high undulator field can be generated and controlled by the solenoid field. However, it is not experimentally proved. We need to check that the BHSAU really generate the sinusoidal magnetic field, i.e., the undulator field. We also have to check that the undulator field amplitude can be controlled well by the solenoid field. The word 'well' means that the amplitude can be changed widely and rapidly (from K = 0 to $K \sim 2$ in several minutes for practical use). Moreover, the applications of bulk HTS have two common problems, namely the cracking and the flux creep. The cracking is caused by the electromagnetic force inside the bulk HTS. The cracking disturb the flow of loop current and/or decrease the critical current density. T. Tanaka, et al., reported that the cracking happened in the demonstration experiment of CU+ [16]. There are some methods to avoid the cracking, for example, addition of silver, resin impregnation or covering by metal ring [33, 34, 35, 36]. We have to check whether the provision against the cracking is required or not for the BHSAU. The flux creep is a temporal decrease of the loop current, caused by the movement and the dissipation of the quantized magnetic flux due

to the thermal excitation and the quantum tunneling. The flux creep has a logarithmic dependence on time, i.e., the current decreases rapidly just after the magnetization and then does gradually. There are methods to suppress the flux creep [37]. It is required to evaluate the degree of the decrease during the field measurement in advance of the other experiments.

In this chapter, the experiments using the six-periods prototype of the BHSAU were performed, to check undulator field generation, tunability of the undulator field amplitude, the effect of cracking and flux creep, In section 4.2, the experimental setup and method for measurement are described. In section 4.3, the experimental results are shown. In section 4.4, the results are discussed.

4.2 Setup

4.2.1 Overview of Prototype

The experimental setup is as follows.

Figure 4.1 shows the prototype of the BHSAU. The prototype features are summarized in Table 4.1. The prototype has the periodic number N of 6, the period λ_u of 10 mm, and the gap g of 4 mm. Twelve bulk HTSs are located in a staggered array configuration, and supported by copper supports in the sample holder. This sample holder is inserted into a cryogenic chamber. The copper support and the sample holder also works as thermal conductor between the bulk HTSs and the cryogenic chamber. The bulk HTS is roughly semi-circular with radius R_s of 12.5 mm; the dimensions in x, y and z are about 24.7, 10.5 and 5 mm, respectively.

Figure 4.2 and 4.3 shows a schematic view and photograph of the experimental setup. The prototype was installed in a cryogenic vacuum chamber, in which the prototype is thermally in contact with a helium pipe. The cryogenic chamber was placed in a 2-T superconducting solenoid aligned so that the central axis of the undulator coin-

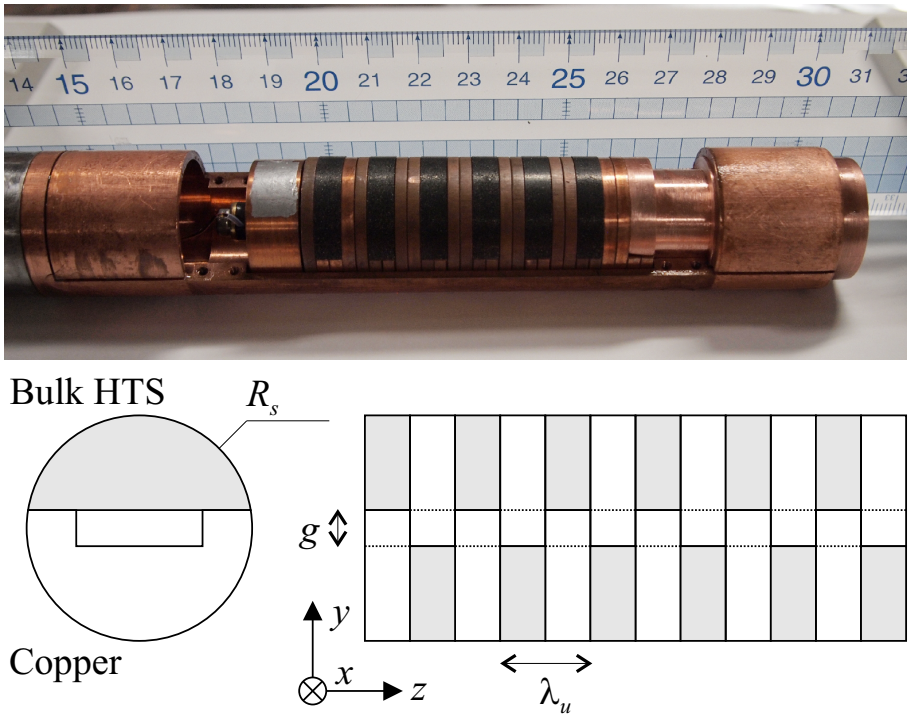

Figure 4.1: Photograph and schematic of six-period prototype (with centimeter ruler). The parameters are $R_s = 12.5$ mm, $\lambda_u = 10$ mm, and $g = 4$ mm. Twelve bulk HTSs were positioned in a staggered array configuration, and supported by the copper support in the sample holder. The origin of the coordinates is set at the geometrical center of the prototype.

cided with that of the solenoid. Cold helium is used to cool down the prototype, and the used helium is reused for the radiation shield. The cooling system of the undulator is independent of that of the superconducting solenoid, and can be changed from around 5 K to over 77 K by helium flow rate and heater current. The speed of the temperature change was about $-$1–2 K / min.

The HTS material is QMG-GdBCO, from Nippon Steel Corporation [32], in which nanoparticles of $\mathrm{Gd_2Ba_1Cu_1O_5}$ (211) are distributed in a $\mathrm{Gd_1Ba_2Cu_3O_{7-\delta}}$ (123) crystal to enhance its magnetic properties in trapping a high field, known as flux pinning.

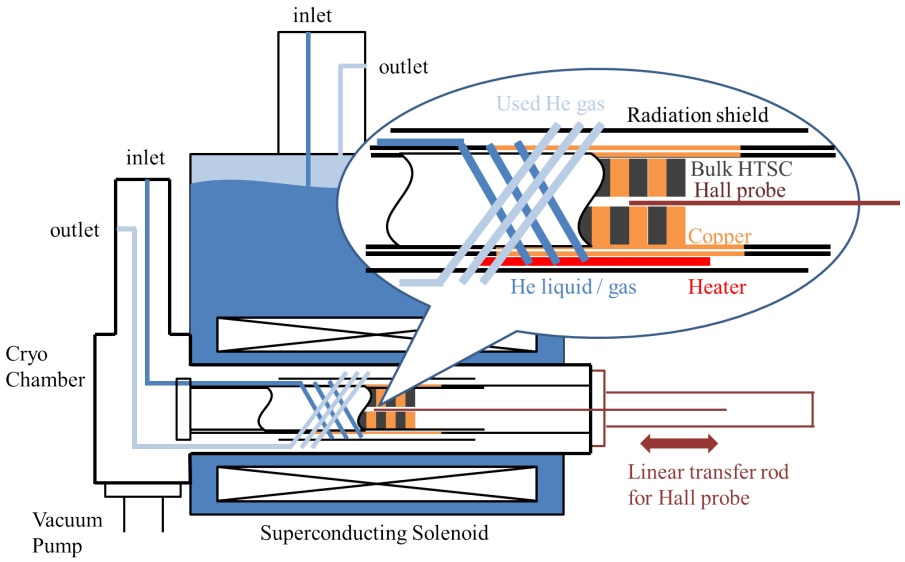

Figure 4.2: Schematic view and photograph of experimental setup. The prototype was installed in a vacuum chamber, in which the prototype is thermally in contact with a helium pipe. The chamber was placed in a 2-T superconducting solenoid aligned so that the central axis of the undulator coincided with that of the solenoid.

Table 4.1: Specification of Prototype

period λ_u [mm]	10
gap g [mm]	4
periodic number N	6
bulk HTS	QMG-GdBCO
bulk dimensions	24.7, 10.5 and 5 mm (xyz)

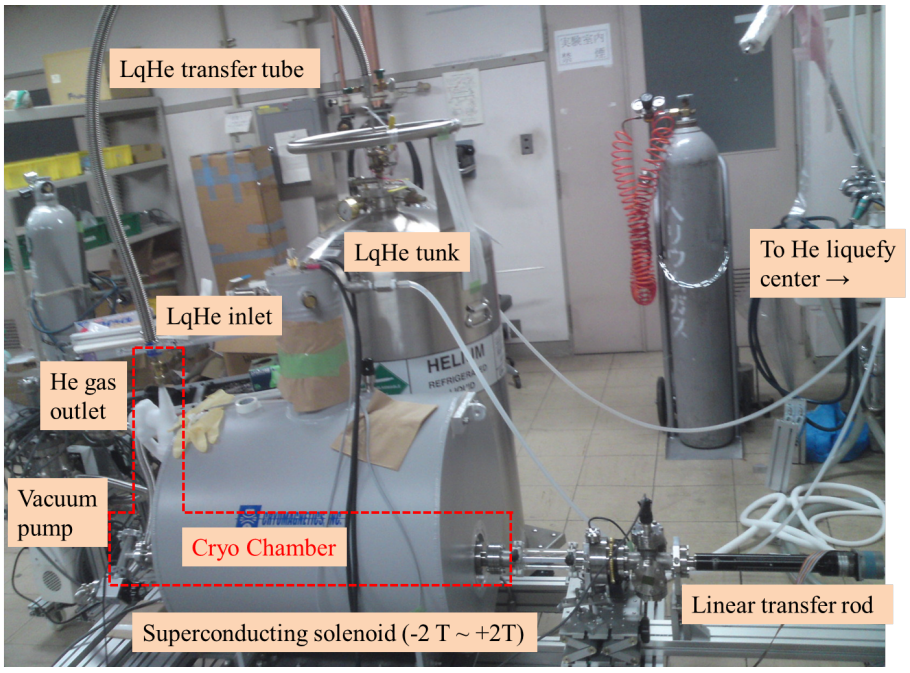

Figure 4.3: Photograph of experiment room.

The critical temperature T_c is around 94 K. The critical current density of a small sample of QMG-GdBCO ($\sim$ 0.2 mm^3) is shown in Fig. 4.4 and Table 4.2. This critical current is calculated from the measured magnetic hysteresis curve (M-H curve). The curve of the small QMG-GdBCO sample is measured by the DC magnetization method (Quantum Design, Physical Property Measurement System with AC measurement system: PPMS with ACMS). The critical current density is derived by the formula:

$$J_c(B) = \frac{4M}{b\left(1-\frac{b}{3a}\right)} = \frac{4}{b\left(1-\frac{b}{3a}\right)}\frac{|m_+(B)-m_-(B)|}{2abc}. \quad (a \geq b)$$

Here $m_+(B)$ and $m_-(B)$ are the upper and the lower point on the hysteresis curve, and $a = 0.6$ mm, $b = 0.4$ mm, $c = 0.8$ mm are the size of the sample; the direction of the applied magnetic field and the dimension c is parallel to the c-axis of the $Gd_1Ba_2Cu_3O_{7-\delta}$ crystal.

As shown in Fig. 4.4 and Table 4.2, J_c of QMG-GdBCO exponentially decreases with an increase of T. J_c also decreases with an increase of B. However, dependency

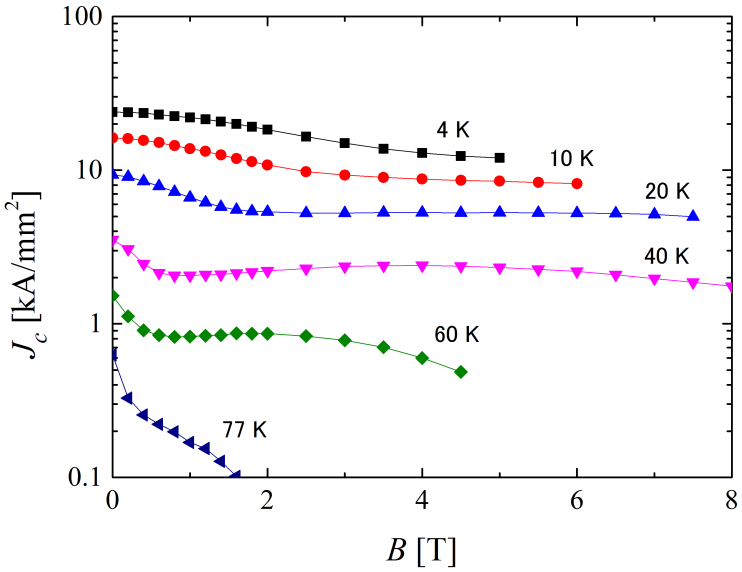

Figure 4.4: Critical current density of QMG-GdBCO under magnetic field. Measured by DC magnetization method with small sample ($\sim$ 0.2 mm^3)

of J_c on B is not as large as that on T. In particular, there are regions in which J_c does not change in wide range of B. For example J_c at $T = 20$ K in Table 4.2 showed the behavior that J_c decreases from 9.4 to 5.4 kA/mm^2 for 2 T change of B, however, J_c remains constant for 4 T change. This is the reason why we employ the approximation of the Beam model, i.e, field independent J_c, in the analysis of the BHSAU. However, for the performance estimation in chapter 6, the dependence on B in the table will be taken into account for reasonable estimation.

4.2.2 Superconducting Solenoid for Magnetization

Table 4.3 shows the specifications of the superconducting solenoid system. The maximum field is $B_s = \pm 2$ T (I_s =25.24 A). The field homogeneity is $\pm 0.1\%$ in 10 mm diameter spherical volume (DSV) and 2% in the prototype volume (cylinder, 80

Table 4.2: Critical current density of QMG-GdBCO under magnetic field. Measured by DC magnetization method with small sample ($\sim$ 0.2 mm^3)

T [K]	J_c [kA/mm^2]			
(T_c = 94 K)	B = 0 T	2 T	4 T	6 T
4	24	18	13	12
10	16	11	8.7	8.2
20	9.4	5.4	5.3	5.3
40	3.5	2.2	2.4	2.2
60	1.5	0.86	0.60	-

mm $\times$ 25 mm diameter). The field ramp rate is calculated from the current ramp rate of the magnet power supply.

4.2.3 Temperature Control System

The temperature is measured with two sensors as shown in Fig. 4.5, a sensor in the sample holder (sensor A, hereafter) and a sensor at the heater place (sensor B). The sensors are Cernox (Lake Shore Cryotronics, Inc.), which have high sensitivity at low temperature and weak magnetic field effect. The helium flow rate and the heater current is used to control the temperature of sensor A. The heater current is controlled by the temperature controller with proportional-integral-derivative (PID) method. Because we started to measure over 30 minutes after the sensor A reached the target temperature, the temperature of the bulk HTSs of the prototype is considered as the equal temperature with sensor A. We haven't calibrated the sensor error caused by the magnetic field. According to the catalog, the error is 0.1% at 2.5 T, 4K or 0.04% at 2.5 T, 20K. The fluctuation of the temperature was kept in a $\pm$0.02% range of the targer temperature during one field distribution measurement, and in a $\pm$0.2% range during several field

Table 4.3: Specification of Solenoid System

Manufacturer	CRYOMAGNETICS, INC.
Field	-2 – $+2$ T ($\pm$25.24 A)
Field Homogeneity	$\pm$0.1% (10 mm DSV)
	2% (80 mm $\times$ 25 mm dia.)
Field Ramp Rate	7.00 mT/s ($\leq$ 1.57 T)
	3.96 mT/s ($\geq$ 1.57 T)
Current Accuracy	4 digits
Current Ramp Rate	0.0884 A/s ($\leq$ 20 A)
	0.0500 A/s ($\geq$ 20 A)
Room Temperature Bore	76 mm

distribution measurements for the measurement of dependence on the solenoid field.

4.2.4 Magnetic Field Measurement System

A Hall-effect probe and a gaussmeter (Lake Shore Cryotronics, Inc., HGCT-3020 and Model 460) were used to measure y-component of the magnetic field along the z-axis $B_y(z)$. The probe was calibrated in the field range from -2 to 2 T and over

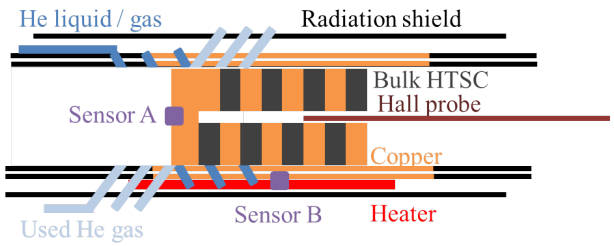

Figure 4.5: Location of the two sensors. Sensor A and B are in the sample holder and the heater place, respectively.

a temperature range from 5 to 300 K. The calibration residual δB_y^{R} is $\pm 0.5\%$. The temperature of the probe at the measurement time is assumed as the equal temperature with the sensor A. The probe is on the handmade probe holder and moved by a linear transfer rod (MDC Vacuum Products, LLC, Lin.MotionFT, 2.75"Flg, 6"Tvl, Spc-D). The measurement increment in the z-direction was 0.5048 mm. The probe error due to the fluctuation of the displayed value of the gaussmeter δB_y^{G} is about $\pm 0.2\%$. The inaccuracy of the vertical position due to the manufacturing error of the handmade probe holder ν_y is at most ± 0.3 mm. There may be no effect of sagging because the probe is placed just on the surface of the lower array of HTSs and copper supports to keep the vertical position. The error due to the inaccuracy of the vertical position δB_y^{V} is given by the formula:

$$\delta B_y^{\mathrm{V}} = \cosh(2\pi\nu_y/\lambda_u). \tag{4.1}$$

By substituting $\nu_y = \pm 0.3$ mm, δB_y^{V} is from 0 to $+1.8\%$. The origin of the longitudinal position ($z = 0$) is obtained from the position of the field peaks. The inaccuracy of the longitudinal position arise from the sagging of the probe holder and the inaccuracy of the angle of the stepping motor. The sagging may not be large because the probe holder touched on the upper surface of the lower magnets and is moved by pulling in one direction. The inaccuracy of the angle of the stepping motor is at most the half step, $\pm 13\mu$m. Moreover, if there is 0.1 mm error, non-contiguous wave form may be observed in the 0.5048 mm step measurement. Therefore, the inaccuracy of the horizontal position ν_z is at most 0.1 mm. By using the equation $\sin(k_u(z+\nu_z))/\cos(2\pi z/\lambda_u)$, the error due to that is $\pm 0.2\%$ at the peaks ($z = \pi/2 + n\pi$). The error due to the finite volume of active area δB_y^{A} is given by the formula:

$$\delta B_y^{\mathrm{A}} = \frac{1}{2r_A \sin(k_u z)} \int_{-r_A}^{+r_A} \sin(k_u(z+z'))\mathrm{d}z' = \frac{\sin(k_u r_A)}{k_u r_A} \tag{4.2}$$

and thus, about -1.6%. Here, $r_A = 0.5$ mm is the radius of the active area, and a perfect sinusoidal field with a wavenumber k_u is assumed. The tilt angle between the

probe and the z-axis also cause the error. The angle can be derived by measuring the solenoid field without activating BHSAU. B_y was constant over z scan and less than 0.02 T at $B_s = 2$ T. Thus, the angle θ was less than 0.6 degree. The error δB_y^{T} is given by

$$\delta B_y^{\mathrm{T}} = \cos\theta - 1 + \frac{B_z}{B_y}\sin\theta \approx -\frac{\theta^2}{2} + \frac{B_z}{B_y}\theta. \tag{4.3}$$

The first term is much less than 0.1% and negligible for this discussion. The second term can be large depending on B_z/B_y. Here B_z is the sum of the the solenoid field B_s and B_z generated by bulk HTSs. The component B_s can be eliminated from the measured data as background offset. From Formula (3.13), B_z component generated by bulk HTSs is zero for the condition in chapter 3. Even for finite period, $B_z/B_y < 1$ may be reasonable assumption. Then δB_y^{T} is up to about 1%.

The total probe error for the field distribution measurement $\delta B_y^{\mathrm{scan}}$ can be estimated by the formula:

$$\delta B_y^{\mathrm{scan}} = \sqrt{\left(\delta B_y^{\mathrm{R}}\right)^2 + \left(\delta B_y^{\mathrm{G}}\right)^2 + \left(\delta B_y^{\mathrm{V}}\right)^2 + \left(\delta B_y^{\mathrm{H}}\right)^2 + \left(\delta B_y^{\mathrm{A}}\right)^2 + \left(\delta B_y^{\mathrm{T}}\right)^2} \tag{4.4}$$

and thus, is less than 4%. Some errors include systematic errors, and then can be removed for future precise measurement if we carefully check the probe errors. We ignored the probe error due to the inaccuracy of position and the active area in x-direction because the undulator field almost the same around $x = 0$.

In the measurement for the flux creep, the probe was fixed at the center of the prototype and the only relative change from the maximum field is used. Therefore the probe errors due to the position and the angle inaccuracies, and the finite volume of the active area can be ignored. Furthermore the measured field range is only around the certain maximum field, thus the effect of calibration residual is also thought to be small. The total probe error for the flux creep measurement is only from the gaussmeter as:

$$\delta B_y^{\mathrm{scan}} = \delta B_y^{\mathrm{G}}. \tag{4.5}$$

Table 4.4: Experimental Equipment

Name	Manufacturer	Model Number
Bulk HTS	NIPPON STEEL [1]	QMG-GdBCO
Gaussmeter	Lake Shore [2]	Model 460
Hall-Effect Probe (B_y)	Lake Shore	HGCT-3020 (Serial H049852)
Superconducting Solenoid	CRYOMAGNETICS [3]	Custom-ordered (Table 4.3)
Solenoid Power Supply	CRYOMAGNETICS	Model 4G-100
He Level Meter	CRYOMAGNETICS	LM-500
Cryogenic Vacuum Chamber	NIKI GLASS [4]	Custom-ordered (Fig. 4.2)
Temperature Controller	Cryo-con [5]	Model 32B
Temperature Sensor	Lake Shore	Cernox CX
Linear Transfer Rod	MDC [6]	Lin.MotionFT, 2.75"Flg, 6"Tvl, Spc-D

and thus, about 0.2%.

4.2.5 List of Equipment

The equipment mentioned above and the other equipment are summarized in Table 4.4.

4.3 Result and Discussion

4.3.1 Flux Creep

To check the effect of the flux creep, the temporal change of the B_y was measured at the center of the prototype just after the magnetization. Because the effect is larger at high temperature and high field, the temperature was set as T = 60 K and B_s was changed from +1.5 to +2 T. The temporal decrease in B_y due to the flux creep after the rapid ramp of B_s was measured.

Fig. 4.6 shows the temporal change of the B_y at the center of the undulator after

the solenoid field is swept from 1.5 to 2 T. The black dots shows the ratio of measured $B_y(t)$ and $B_{y0} = B_y(0)$. Here we defined $t = 0$ is the time that the B_y takes the maximum during or just after the solenoid field change. The green line shows the fitted line with the formula:

$$\frac{B_y}{B_{y0}} = 1 - A \log\left(\frac{t}{t_0} + 1\right) \tag{4.6}$$

Here, A is the decay constant and t_0 is the time constant for the decay. The fitted result was $A = 0.01854 \pm 1.04389 \times 10^{-5}$ and $1/t_0 = 6.81196 \pm 0.01649$. The adjusted coefficient of determination was $R'^2 = 0.99862$.

From the above result, we found that although any suppression method of flux creep should be used in the real machine, it is negligible for the field distribution measurements in the following section. Let us discuss the detail. In Fig. 4.6, we used the (4.6) for fitting because of the following reason. The temporal decrease of the critical density J in the flux creep state is expressed by

$$\frac{J}{J_{c0}} = 1 - \frac{k_B T}{U_0^*} \log\left(\frac{t}{t_0} + 1\right) \tag{4.7}$$

Here k_B is Boltzmann constant, $J_{c0} = J(t = 0)$, and U_0^* is the effective pinning potential. B_y is determined by J and the region of the current flowing. In the flux creep, the region volume is not changed. Thus the temporal change of B_y may show a similar trend to that of J. With the fitted data $A = 0.01854$ and $T = 60K$, we obtained $U_0^* \sim 0.28$ eV. This value is reasonable. This means that the temporal decrease obeyed the law of the flux creep; therefore, we can apply the methods of the flux creep suppression to suppress this decrease.

The decreasing ratio is not small at this temperature and field. The field decrease by around 7% after 1000 minutes. The most serious problem is the rapid decrease after the magnetization. However, we ignored the effect of the flux creep in the following results and discussions because of the following reasons. First, we made the field distribution measurement in the following section from t = 5 minutes to t = 15 minutes after the

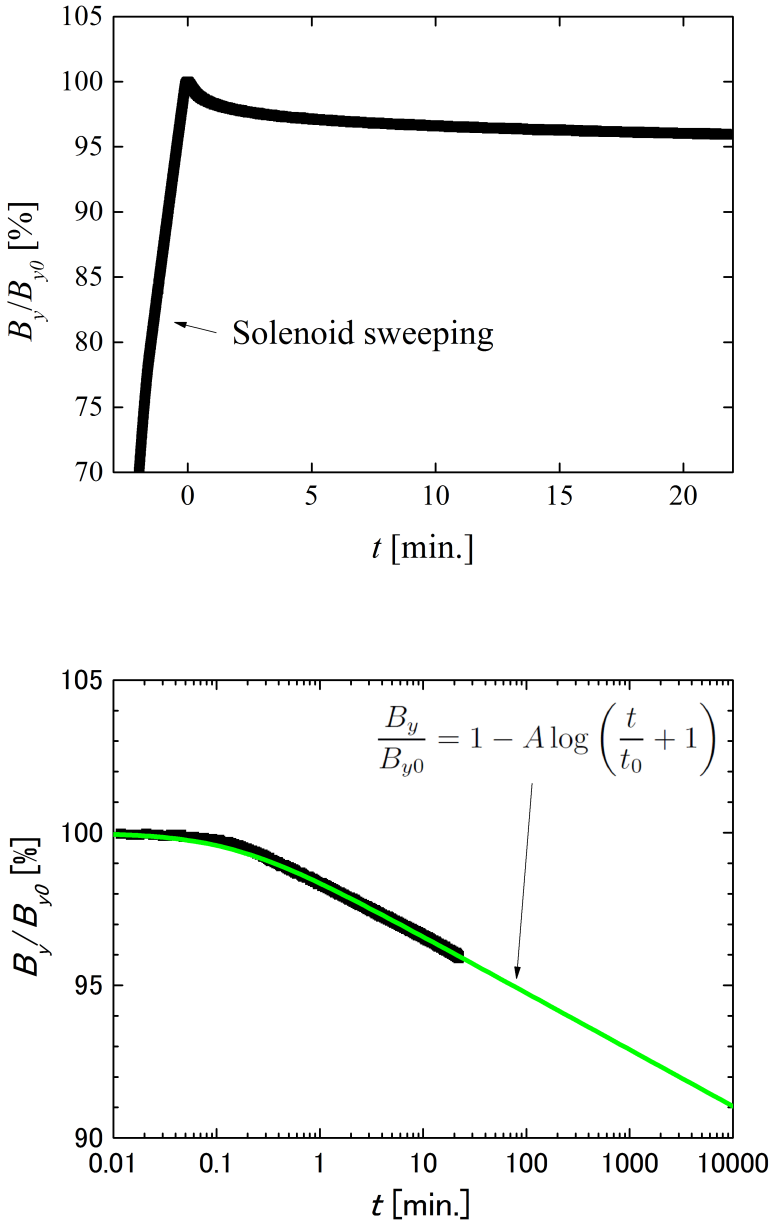

Figure 4.6: The temporal change of the undulator field amplitude at the center of the prototype. The temperature was T = 60 K and B_s was changed from +1.5 to +2 T.

magnetization, to avoid the rapid decrease near t = 0. Thus, we can consider that the maximum absolute decrease was about 3.7% after the measurement and the relative decrease during the measurement was about 0.8%; this is less than the probe error at the field distribution measurement. Second, the effect is much smaller at 20 K and 40 K or under the lower field than 2 T. However, the stability of the undulator field is crucial for the use of the undulator radiation. Thus, in the future study, we have to discuss the application of the method to suppress the flux creep [37].

4.3.2 Field Distribution Example

The vertical field distribution along z-axis $B_y(z)$ is measured at 6, 20, 40, 60K.

Figure 4.7 shows the example of the vertical field distribution along z-axis $B_y(z)$. The prototype was cooled down with the solenoid field of $B_s = -2$ T. The measurement was done with $B_s = 0$ T and $T = 20$ K. The sinusoidal magnetic field, i.e., undulator field, was successfully observed. The undulator field amplitude B_0 was calculated from the formula:

$$B_0 = \frac{1}{4}\sum_{n=1}^{4}\frac{|P_n - P_{n+1}|}{2}. \tag{4.8}$$

Here $P_n(n = 1 \cdots 5)$ are 5 central peaks (near $z = -10, -5, 0, +5, +10mm$) of the cubic-spline fitted data of the measured field distribution. The undulator field amplitude B_0 was about 0.47 T. and the relative standard deviation ν was 0.46%.

There were two large peaks at the both end of the field distribution (near $z = -25, +25$ mm). These peaks were, respectively, -0.74 and -0.71 T.

From the above result, we found that the sinusoidal magnetic field was generated in the BHSAU. The variation of the center peaks is smaller than the measurement error. Thus, it is difficult to discuss the accurate field uniformity, however, it is not so large without any field correction such as magnet sorting. We tolerated 15% individual differences of the critical current density of the bulks at shipment time, while it can

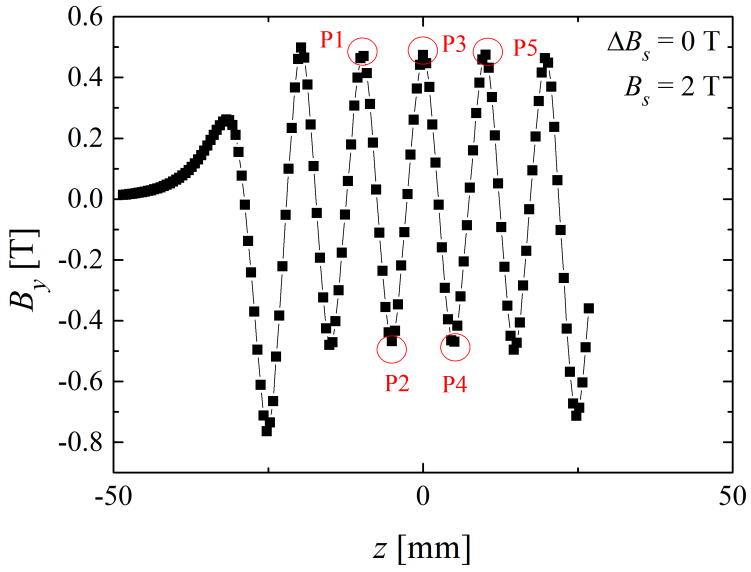

Figure 4.7: Vertical field distribution along z-axis. The five peaks from P1 to P5 are used to derive the amplitude of the undulator field B_0.

be reduced by performing triage. Furthermore, the critical current density was inhomogeneous in the sample. The reason why the variation of peak field were much less than the individual differences is the following. The bulks have almost the same intensity of magnetization independently of its critical current density. From Bean's critical state model, the current density in the bulk HTS is equal to the critical current density ($J = \pm J_c$) or zero ($J = 0$), and current starts flowing from the outer periphery of the bulk to negate the field change inside the bulk. In a low-J_c bulk, the current-flowing layer is large; in a high-J_c bulk, the current-flowing layer is small. Therefore, the bulks have almost the same intensity of magnetization; the variation of peak field was reduced to much less than the individual difference of bulks. Quantitative discussions are difficult with the measured data; thus we introduce related numerical results [38]. Although only one bulk was assumed to have a different critical current density from the others, the calculation showed that the difference between the peak amplitude near the

bulk and the average amplitude is suppressed to 1/7–1/5 in the difference of the critical current density. The experiment result was consistent with the numerical calculation. This phenomenon that the appearance of the individual difference of magnets to the undulator field is automatically suppressed, is not seen in other undulators and can be an advantage of the BHSAU. Particularly in the high-field undulator, because the absolute field error to be corrected is also high, the field correction based on the intrinsic property of superconductor, which has an effect at a constant rate in any critical current density, is important.

The situation is different when current flows almost everywhere in the bulk, i.e., saturation. Due to the finite volume of the bulk, the amount of loop current is limited by volume and J_c. As the intensity of magnetization of the bulk, which has lower J_c, approaches saturation, the difference in magnetization between low-J_c and high-J_c bulks become larger. Investigation of the field correction method using the knowledge about HTS will be an important topic especially if the BHSAU is used under a condition close to saturation.

4.3.3 Solenoid Field Dependence

Measurements were performed under zero-field cooling (ZFC) and field cooling (FC) conditions. These are implemented by controlling the bulk HTSs temperature and the solenoid field independently as follows. In ZFC, the solenoid field B_s was zero before superconducting transition of bulk HTSs, and changed to target value after cooling bulk HTSs down to the measurement temperature. In FC, B_s of non-zero value, for example -2 T, was applied before the transition, and changed to target value after cooling. We define ΔB_s as the change in solenoid field before transition and at measurement, and B_{s0} as the initial B_s before transition. For instance, ΔB_s = 3 T at B_s = +1 T under FC ($B_{s0} = -2$ T) conditions.

Figure 4.8 shows the vertical field distribution along z-axis $B_y(z)$ with changing the

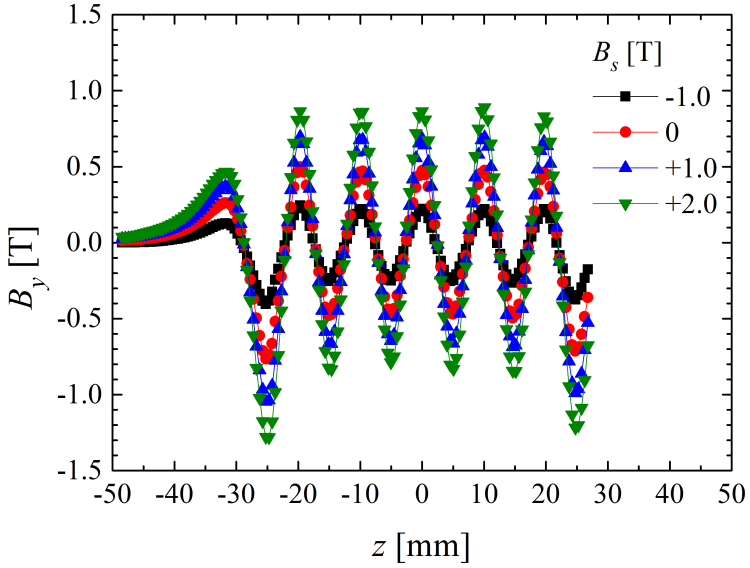

Figure 4.8: The field distribution under the various solenoid field. The amplitude of the field increased with ΔB_s.

solenoid field. The prototype was cooled down with the solenoid field of $B_s = -2$ T. The measurement was done with $B_s = -1, 0, +1, +2$ T and $T = 20$ K. All vertical field distribution were geometrically similar.

Figure 4.9 shows the B_0 dependence on B_s. The prototype was cooled down under ZFC and FC ($B_{s0} = -2$ T) condition. The measurement was done with $T = 6$ K. All vertical field distribution were geometrically-similar.

From the above result, we found the following. The undulator field reached 0.85 T. This value is higher than that of IVU. The undulator field amplitude can be controlled by the solenoid field.

The time to change the undulator field from 0 to 0.85 T ($K \approx 0.8$) was about 10 minutes except B_y measurement time. This depends the factory-preset field ramping rate of the solenoid shown in Table 4.3. Because increase of the temperature of bulk HTSs was not observed during the field ramping, the ramping rate can be increased and

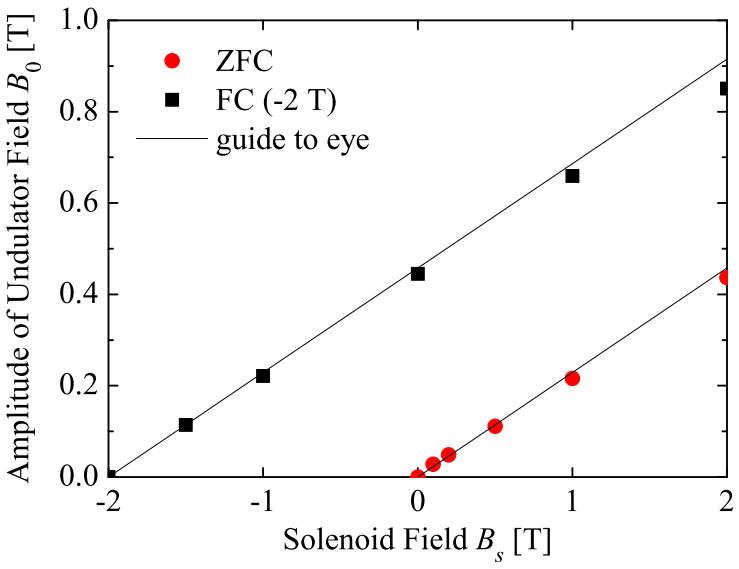

Figure 4.9: The dependency of B_0 on B_s. The measurement were performed with the ZFC ($B_s = 0$ T at first) and FC ($B_s = -2$ T at first) conditions. Two parallel lines are for the guide to eye.

the time to require field tuning will be at most several minutes. For PMU, the time to change the undulator field from zero to $K = 1$ is about one minute. The time for the field tuning in BHSAU is as rapid as comparable with the conventional undulator.

From the B_0 dependence on B_s under both ZFC and FC conditions, we found the following. In Fig. 4.9, B_0 at B_s = +2 T for ZFC and B_0 at B_s = 0 T for FC are almost the same, where ΔB_s is 2 T under both conditions. In other words, B_0 was independent of B_s but dependent on ΔB_s. This result is explained as follows. Because the critical current density of QMG-GdBCO does not have a large field dependence at 6 K [39], the critical current density at any point in any bulk HTS is almost constant irrespective of the field at the point. In the case when ΔB_s monotonically increases, since the current density is the same as the critical current density, the amount of loop current and its distribution inside the bulk HTS are always the same whenever ΔB_s is the same. Because the y-component of the field is only generated by the current in bulks, B_0 therefore depends not on B_s but on ΔB_s.

In the case when ΔB_s decreases from a certain point, B_0 decreases with a decrease of ΔB_s. The loop current in inverse direction starts flowing from the periphery of the bulk and the loop current in the original direction flows inside of the bulk. Thus, the B_0 curves at the increase and the decrease of ΔB_s are different in a precise sense.

From the above results, one easily finds that any combination of the solenoid field before and after the superconducting transition can generate an undulator field corresponding to ΔB_s. This brings two benefits: one is that the required solenoid field to generate the same strength in the undulator field can be reduced by a factor that is half for FC; the other is that B_z under operating conditions in an accelerator is tunable because B_z depends on B_s and ΔB_s. This has potential in resolving the largest problem of conventional staggered-array undulators, stemming from using only soft-ferromagnetic pieces. The problem is the undesirable divergence of the electron beam when B_z is strong. However, to reap both benefits, further investigation, for example

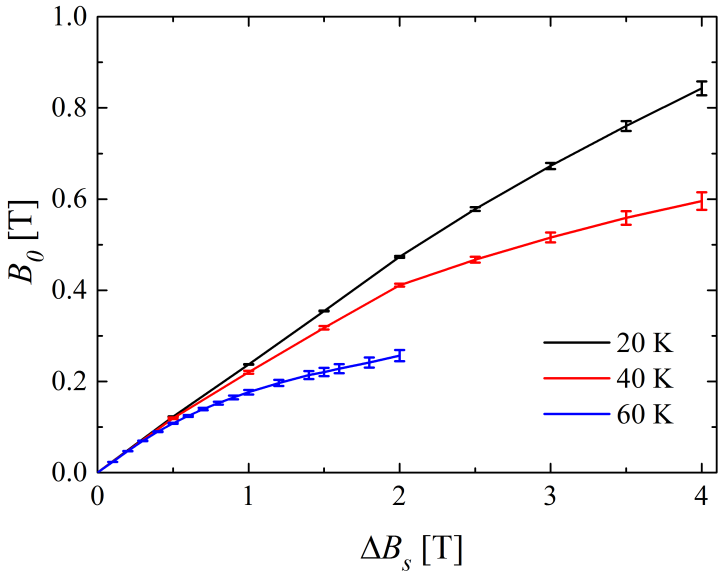

Figure 4.10: Dependence of ΔB_s-B_0 curve on temperature. The measurement was done with FC ($B_{s0} = -2$ T) condition at $T = 20, 40$ K, and ZFC condition at $T = 60$ K

on the variation in B_z, is required.

4.3.4 Temperature Dependence

Figure 4.10 shows the dependence of ΔB_s-B_0 curve on the temperature. The measurement was done with FC ($B_{s0} = -2$ T) condition at $T = 20, 40$ K, and ZFC condition at $T = 60$ K. The initial gradient $\mathrm{d}B_0/\mathrm{d}\Delta B_s|_{\Delta B_s=0}$ was found to be about 0.24 at any temperature. The gradients of the curves show the decrease at high ΔB_s. The curve of the lower temperature is higher than that of the higher temperature.

From the above results, we found that the experiment result shows similar behavior with the result of theoretical analysis, i.e., that the gradients were the same at any temperature and that the curve of the lower temperature is higher than that of the higher temperature. This means that the description of the theoretical model is correct, in

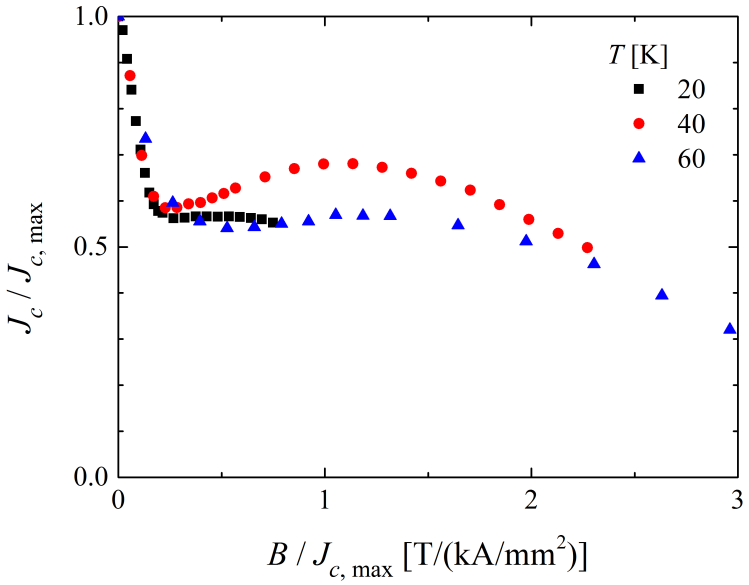

Figure 4.11: Normalized critical current density of QMG-GdBCO. The both J_c and B is normalized by $J_{c,\max}$ at each temperature.

which the current starts to flow from the periphery of the bulk HTSs and the depth of the current-flowing layer increase with an increase of ΔB_s.

The only exception is in case of that the current distribution at each different T has different shape under equal $\Delta B_s/\Delta B_{s,\max}$. This is caused if $J_c - B$ curve has large shape change depending on T. However, we found that the curves in Fig. 4.11 from the DC magnetization method did not show large shape change depending on T and also the effect did not appeared on the initial gradients measured in chapter 4.

4.3.5 Cracking

No phenomena related to cracking was observed. It was confirmed by that the field distribution was not changed largely if the amplitude was changed and has the reproducibility at the same experiment condition after warm up. It is not clear whether or

not any cracking will not occur in the BHSAU after multiple use. However, it is worth while to investigate the detail.Tanaka et al. reported that the crackings happened with many samples in their experiment of CU+ at 77 K and under the magnetic field of below 2 T [16]. We used the same bulk HTS, QMG-GdBCO, from the same company, Nippon Steel Corporation, with them. The critical current density of their experiment might be over 10 times lower than that in our experiment at 6 K and the applied magnetic field was almost the same. Then, the magnetic force in the bulk HTS might be over 10 times smaller than our experiment.

While Tanaka et al. observed the cracking in CU+, we didn't observed any cracking. One reason is that, in CU+ the bulk HTSs of upper and lower series are moved against the attractive force of each other with only the two point are held. Another is that, in the BHSAU the inner wall of the sample holder make the compressive force to bulk HTSs because of the difference of coefficient of thermal expansion between copper and bulk HTS. This is the way commonly used also in other bulk HTS applications. The other is that, because we used helium and it took a long time (about two or three hours) to cool down the prototype, thermal shock due to the temperature difference in bulk HTS was small.

4.4 Conclusion

This is the first ever experimental study of the BHSAU. The most important conclusion of this study is that the high undulator field generation and the good and rapid tunability of the field (from K = 0 to $K \sim 1$ in 10 minutes) are demonstrated in the experiment by using the prototype of the BHSAU. The measured undulator field 0.85 T is higher than that of the same period and gap IVU. Higher undulator field can be expectable by using the stronger solenoid. The undulator field can be controlled from 0 to 0.85 T by changing the solenoid field change from -2 to 2 T. Although the flux creep

was observed, it was negligibly small for the measurements in this study. No cracking was observed during the experiment.

The knowledge of this study is useful for the future experiment and also for the validation check of the numerical simulation results. The future perspectives of experimental study are, for instance,

1. More precise measurement of the field strength and distribution to check field uniformity and high-harmonic components, because they affects the properties of undulator radiation. Also with the precise field distribution, validation of the analytical or numerical models can be made with the distribution, whereas now only amplitude of the field is compared.

2. Measurement of the z-component of the field inside the prototype.

3. Measurement of the long term stability of the undulator field at multiple points to check the change of the field profile, which occur if the current degradation rate due to the flux creep are different at each point.

Chapter 5

Numerical Calculation of BHSAU

5.1 Introduction

In chapter 3, we introduced the simple analytical model of BHSAU. That model considers the two-dimensional space (the infinite structure in x-direction) and the infinite periodic number in z-direction. However, real undulators have the finite sizes. For the design of the undulators, three-dimensional magnetstatics computation codes are commonly used. For example, RADIA [40], which was developed in ESRF Insertion Device Laboratory, is commonly used to design undulators using PMs, nonlinear soft magnet materials, and/or electromagnetic coils.

For an undulator using bulk HTS, the conventional methods cannot be used because of the difficulty of calculating the magnetization of bulk HTSs. The superconducting loop current inside a bulk HTS depends on the critical current density J_c, the current distribution, and the history of the applied field after the superconducting transition. To further complicate matters, J_c at a certain point in a bulk HTS depends on the magnetic field at the point. To calculate the magnetization of bulk HTSs, there are multiple steps depending on the required accuracy. The first step is to use a simple current distribution that does not vary in the z-direction and a constant J_c corresponding to the average

critical current density in all bulk HTSs. The second is to use a current distribution that varies in the z-direction and a constant J_c. The third is to use a current distribution that varies in the z-direction and with a J_c that depends on the field. And the more extensional treatments of bulk HTS can be considered. However, it is not clear that which step of study is required to sufficiently investigate the field property of BHSAU.

In this chapter, a three-dimensional numerical model of the BHSAU is proposed based on Bean's critical state model. The two methods named center field (CF) method and energy minimization (EM) method are used to determine the current distribution in the numerical model. The former assumes a constant J_c and a simple current distribution as a natural extension of the analytical model to three-dimensional geometry. The latter assumes a constant J_c and the current distribution that varies in the z-direction inside each bulk HTS so that the magnetic energy is minimized. Comparison of results obtained by these two methods may reveal the effect of the current distribution on the undulator field calculation. In section 5.2, three-dimensional model of bulk HTS and BHSAU, the CF method, and the EM method is introduced. The numerical computation methods of them are also described. In section 5.3, the results of the numerical calculation are shown. In section 5.4, mainly discussed are the differences in the results obtained by two methods and the importance of treating the current density. In section 5.5, we make the conclusion of the numerical study and give the future perspectives of the numerical study. The quantitative evaluation of the numerical models are made with the experimental results in the next chapter.

5.2 Three-dimensional Numerical Model of BHSAU

5.2.1 Overview

The numerical model of BHSAU consists of the three-dimensional representation of the bulk HTS and the two methods to determine the current distribution in that. The

bulk HTS is represented by a set of current loops. The two methods determines the loops in which the current flows or does not flow.

5.2.2 Three-Dimensional Representation of Bulk HTS

The path of the loop current inside the bulk is fixed and spatially-discretized. Figure 5.1 shows the three-dimensional representations of the rectangular bulk (upper) and D-shape bulk (lower). The rectangular bulk is used for the comparison of the two methods and the comparison with the analytical calculation. Because a sufficiently large D_x ($D_x = 10\lambda_u$) is assumed for the rectangular bulk, the calculation geometry is similar to that used in the two-dimensional analytical calculation ($D_x \to \infty$). The D-shape bulk is the same shape as the bulk used in the experiment ($R = 12.5$ mm). The left figures are cross sectional views in the yz plane and the right figures are cross-sectional views in the xy plane. Here, N_z and N_y are the numbers of divisions of the bulks in the z- and y-direction, respectively. The stars indicate the center of the bulks. We assumed that the loop current flows only in the plane perpendicular to the z-axis. This is because the z-component is dominant in the solenoid field and in a field generated on a bulk HTS by other bulk HTSs. The loop numbered by ij has the current:

$$I_{ij} = \int_{S_{ij}} J_c(\mathbf{B})\ \mathrm{d}S.$$

Here, S_{ij} is the cross sectional area of divided area. According to the assumption of Bean's critical state model for a type-II superconductor, the critical current density is constant throughout the bulk; thus, each loop has an equal current:

$$I_{ij} = \frac{I_c = J_c^{\mathrm{bulk}} D_z D_y}{2N_z N_y}.$$

5.2.3 Geometry of Calculation

In the numerical calculations, single bulk HTS or $2N$ bulk HTSs for N periodic number are located in the coordinates as shown in Fig. 5.2 or Fig. 5.3. In Fig. 5.2, the

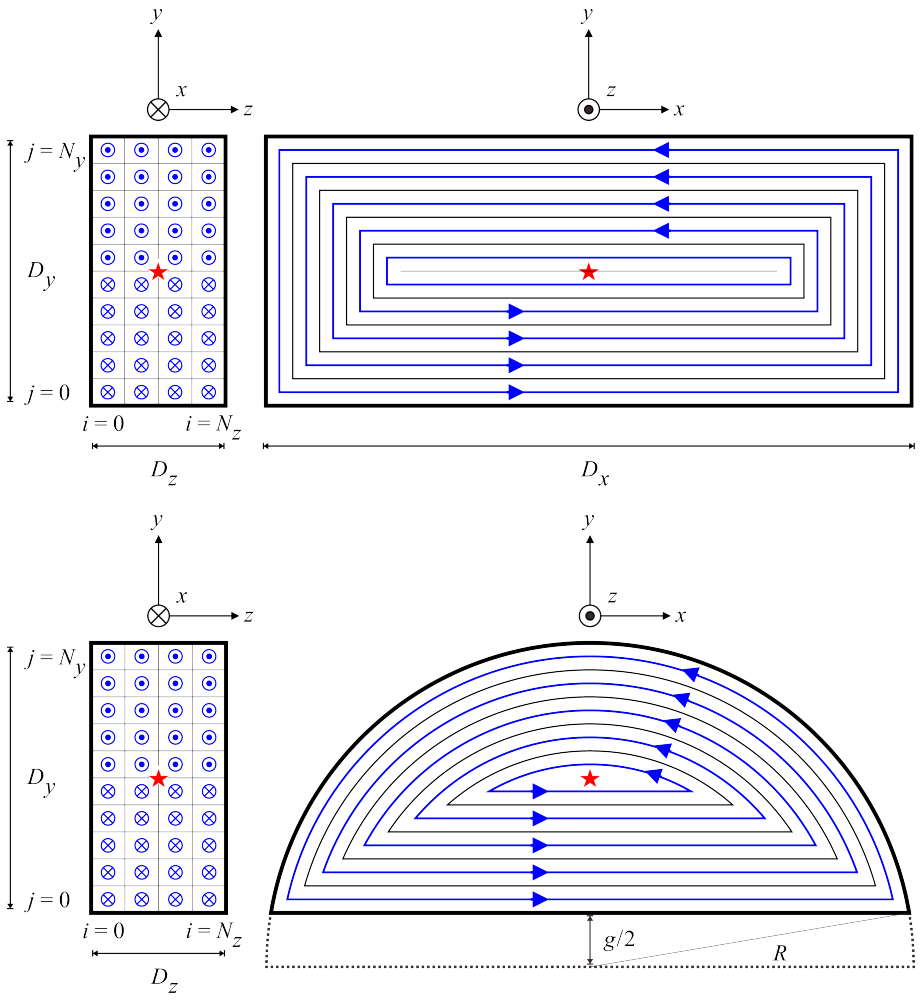

Figure 5.1: Loop Current Model of Bulk HTS.

(a) Rectangular bulk (upper) (b) D-shape bulk (lower). The bulk HTS is represented by N_y times N_z loops with fixed geometry. The stars indicate the centers of the bulk HTSs.

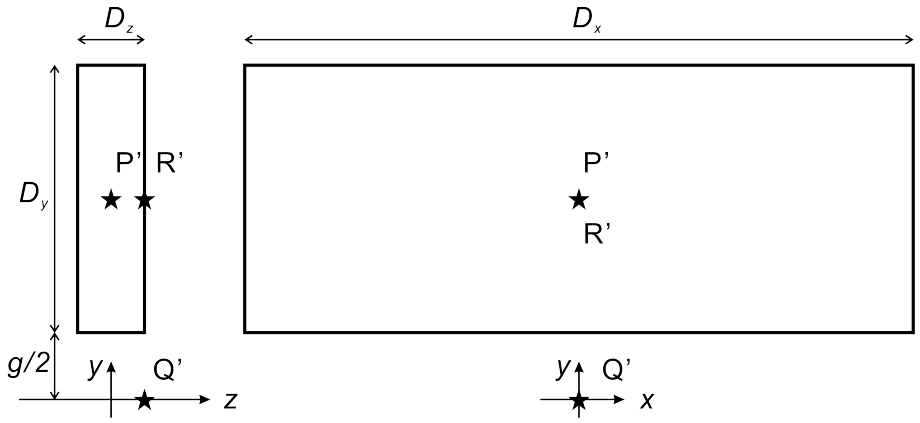

Figure 5.2: Geometry for single bulk HTS. The points P', Q', and R' are observation points.

observation points we use later are shown. The points P' and R' are the center of the bulk HTS, the center of the surface of bulk HTS, respectively. The point Q' is on the z-axis and at the same z-position with the point R'.

The solenoid field is given as the z-direction uniform background in infinite calculation space. As shown in Fig. 5.3, the positions of the bulk HTSs are fixed by the period, λ_u, independent from the thickness of the bulks, D_z. The first figure is for $D_z = 0.5\lambda_u$ $(f = 0.5)$. The second figure is for $D_z = 0.8\lambda_u$ $(f = 0.2)$.

5.2.4 Center Field Method

The basic idea of the center field method (CF method) is the same as that used in the analytical calculation. The loop current flows to negate the change in the solenoid field at the center of the bulk.

The key differences of this method from the analytical calculation are the finite periodic number and, for the D-shape bulk, the three-dimensional geometry. Because of the finite periodic number, we assumed that each bulk HTS has a different depth at which the current flows, $d_{y,G}$ $(G = 1, \ldots, 2N)$. Here, N is the periodic number of

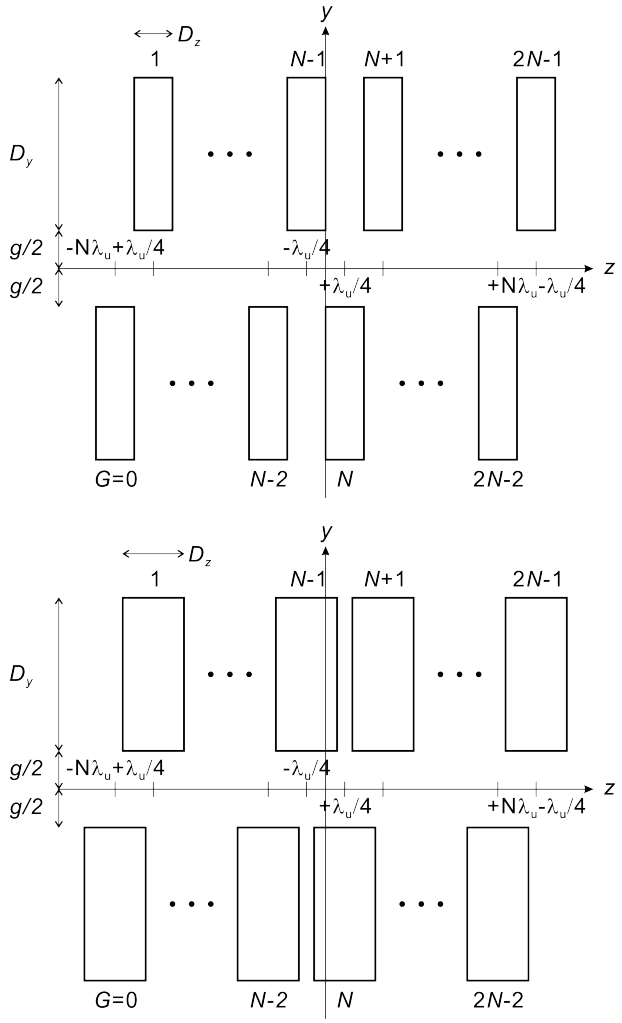

Figure 5.3: Geometry for N-periodic-number BHSAU. The first figure is for $D_z = 0.5\lambda_u$ $(f = 0.5)$. The second figure is for $D_z = 0.8\lambda_u$ $(f = 0.2)$.

the undulator and $2N$ is the number of the bulks. We also assumed that each depth is determined by the change in B_z at the center of each bulk HTS, $B_z(\mathbf{r}_{c,G})$. By defining $\mathbf{B}_{GH}$ as the magnetic field generated by the Hth bulk at the center of the Gth bulk, we obtained $B_z(\mathbf{r}_{c,G})$ as

$$B_z(\mathbf{r}_{c,G}) = \left[\sum_{H=1}^{2N} \mathbf{B}_{GH}(d_{y,H})\right]_z. \tag{5.1}$$

By using the assumption $B_z(\mathbf{r}_{c,G}) = -\Delta B_s$,

$$\left[\sum_{H=1}^{2N} \mathbf{B}_{GH}(d_{y,H})\right]_z + \Delta B_s = 0. \tag{5.2}$$

To determine all $d_{y,G}$, the iterative computation was performed.

In the computation, d_y is discretized by n_y. Here, n_y is the discretized depth of the layer in which the current flows ($0 \leq n_y \leq N_y$). Moreover, to obtain a high-precision result with a small number of divisions in the y-direction (N_y), we assumed that the current I_c flowed in n_y lines and that a current of αI_c $(0 \leq \alpha < 1)$ flowed in the $(n_y + 1)$th line. Here, α is calculated from the residual $\Delta B_s - B_z(\mathbf{r}_{c,G})$ in each iteration. Then, the field at the center of the Gth bulk generated by loop ij in Hth bulk is obtained using the discretized Biot-Savart law:

$$\mathbf{B}_{GHij} = \frac{\mu_0 I_c}{4\pi} \sum_{p=1}^{N_c} \frac{\Delta \mathbf{s}_p \times \mathbf{r}}{r^3}. \tag{5.3}$$

Here, N_c is number of the line elements (the number of divisions of the loop), $\Delta \mathbf{s}_p$ is the pth line element of loop ij in the Hth bulk, and r is the distance between $\mathbf{r}_{c,G}$ and the center of the line element. Then, the field $\mathbf{B}_{GH}$ is expressed by

$$\mathbf{B}_{GH}(n_{y,H}) = \sum_{i=1}^{N_z} \left(\sum_{j=1}^{n_{y,H}} B_{GHij} + \alpha B_{GHi(n_{y,H}+1)} \right). \tag{5.4}$$

5.2.5 Energy Minimization Method

The energy minimization method (EM method) was proposed by Badía et al. to determine the critical state in which a system organizes itself [41]. Sanchez and Navau

applied the method to a single bulk HTS with a finite height and cylindrical symmetry [42]. The shielding current distribution of a finite cylinder can be obtained with a constant J_c or field-dependent J_c under a uniform/nonuniform applied field.

In this study, to use the EM method for the three-dimensional problem of bulk HTSs with an arbitrary shape, we assumed the path of the loop current and used the discretized Neumann formula for inductance computation.

The EM method is as follows. The energy required for the current to flow is the sum of the work required for the current to flow against the magnetic field induced by other loops and the energy obtained upon the vanishing of the external field. For current I_{ij} to flow in loop ij, the required energy is written as

$$\begin{aligned} E_{ij} &= I_{ij}\left(\Phi_{ij}^{\mathrm{int}} - \Phi_{ij}^{\mathrm{ext}}\right) \\ &= I_{ij}\left(\sum_{kl}^{N_y N_z} M_{ij,kl} I_{kl} - \int_{S_{ij}} B_{\mathrm{ext}}\,\mathrm{d}S\right). \end{aligned} \tag{5.5}$$

Here Φ_{ij}^{int} is the magnetic flux on the surface surrounded by the loop ij generated by the other loops, Φ_{ij}^{ext} is the magnetic flux on the same surface from the external field, and $M_{ij,kl}$ is the mutual ($ij \neq kl$) or self- ($ij = kl$) inductance between the loops. If a constant J_c is assumed, I_{ij} and I_{kl} are both equal to I_c. The calculation procedure is as follows:

1. Calculate E_{ij} for every loop that does not have a current.
2. Finish the calculation if there is no loop with $E_{ij} < 0$.
3. Find the loop with the minimum E_{ij}.
4. Flow a current in the loop.
5. Repeat the calculation from step 1.

The current distribution after the calculation shows the critical state.

The model can be applied to three-dimensional problems with bulk HTSs of an arbitrary shape if the path of the loop current is determined in advance. We assumed the current path shown in Fig. 5.1 in common with the CF method. The current flows in a fixed plane normal to the z-axis. This is similar to the thin-film approximation used in finite element analysis for bulk HTS. However, in the thin-film approximation, the current path is free in the plane normal to the z-axis; in this model, the current path is fixed in the plane to calculate the inductances in advance.

For a loop current with an arbitrary shape, it is difficult to find analytical formulae for the mutual inductance and self-inductance. Therefore, we numerically calculated the mutual inductance and the self inductance. The vector potential generated by loop kl at position $\mathbf{r}$ is described by the Biot-Savart law:

$$\mathbf{A}_{kl}(\mathbf{r}) = \frac{\mu_0 I_{kl}}{4\pi} \oint_{C_{kl}} \frac{\mathrm{d}\mathbf{s}_2}{r}. \tag{5.6}$$

Here I_{kl} is the current flowing in loop kl and C_{kl} is the loop. The magnetic flux generated by loop kl on the surface surrounded by loop ij is expressed by

$$\begin{aligned} \Phi_{ij,kl} &= \oint_{C_{ij}} \mathbf{A}_{kl} \cdot \mathrm{d}\mathbf{s}_1 \\ &= \frac{\mu_0 I_{kl}}{4\pi} \oint_{C_{ij}} \oint_{C_{kl}} \frac{\mathrm{d}\mathbf{s}_1 \cdot \mathrm{d}\mathbf{s}_2}{r}. \end{aligned} \tag{5.7}$$

By discretizing the formula, we obtain the mutual inductance between loops ij and kl:

$$M_{ij,kl} = \frac{\Phi_{ij,kl}}{I_{kl}} = \frac{\mu_0}{4\pi} \sum_{p}^{N_c} \sum_{q}^{N_c} \frac{\Delta s_{ijp} \Delta s_{klq}}{r_{pq}}. \tag{5.8}$$

Here Δs_{ijp} and Δs_{klq} are respectively the pth and qth line elements of loops ij and kl, r_{pq} is the distance between the centers of the two elements, and N_c is the number of line elements (the number of divisions of the loop). The self-inductance of loop ij is calculated as the mutual inductance between loop ij and a slightly larger copy of loop ij, which is at some distance from loop ij. The distance is $0.78 D_y/2/N_y$. For a torus which has major radius R_{ij} and minor radius $D_y/2/N_y/2$, the calculation using this

distance matches the analytical solution of the self-inductance. For a bulk HTS with an arbitrary shape, we define R_{ij} as the smallest distance in y-direction between loop ij and the center of the bulk HTS (the star in Fig. 5.1).

5.2.6 Details of Computation

The typical values of the divisions used in the computation were $N_y = 200$, $N_z = 50$, $N_c = 1024$–8192. The large number of N_c was required in the computation of the mutual inductances to avoid physically funny current distribution. To compute the mutual inductance in the high precision level with the short computation time, the values of N_c were adjusted by the distance of the two current loops. Many numerical methods were applied to shorten the computation time by using the symmetry and/or the parallel translation invariance of the problems. Furthermore, parallel computations were made for the computations of the mutual inductances. The combination of OpenMP and MPI, so-called 'Hybrid MPI', was used to allow large memory to one MPI process by sharing the memory in the OpenMP threads. The MPI node was consist of 2 of 16 core AMD Opteron 6000 series 2.5 GHz CPU and 64 GB memory. At most 12 nodes, i.e., 384 CPUs were used. The typical computation time for one geometry was about from several hours to three days depending on the geometrical parameters (mainly on the periodic number N) and the number of nodes.

5.3 Result

5.3.1 Single Bulk HTS

Figure 5.4 shows the cross sectional view of the current distribution (x-direction current in zy plane) in bulk HTS by CF method (left) and EM method (right). The rectangular indicates the cross section of bulk HTS in zy plane. The black area indicates

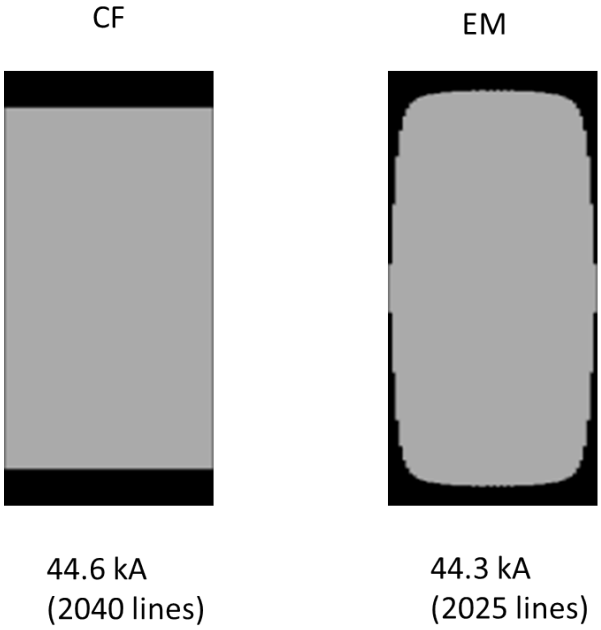

Figure 5.4: Cross sectional view of current distribution (x-direction current in zy plane) in single bulk HTS by CF method (left) and EM method (right).

the current flowing layer. The same z-direction magnetic field of about 2 T is applied to single bulk HTS having $J_c = 10$ kA/mm^2 in both method. The difference of the total current is less than 1%. However, the distributions are much different. In CF method, the current flowing layer has the same depth as is clear from the assumption. In EM method, on the other hand, the depth of current flowing layer is large at the both edge.

Figure 5.5 shows the dependence of B_y at Q' on ΔB_s by CF and EM method. The difference of B_y is large where ΔB_s is small. The both method shows the same B_y at the saturation.

5.3.2 Current Distribution and Undulator Field in BHSAU

Figure 5.6 shows the cross sectional view of current distribution (x-direction current in zy plane) in BHSAU by EM method. The depth of the current flowing layer at

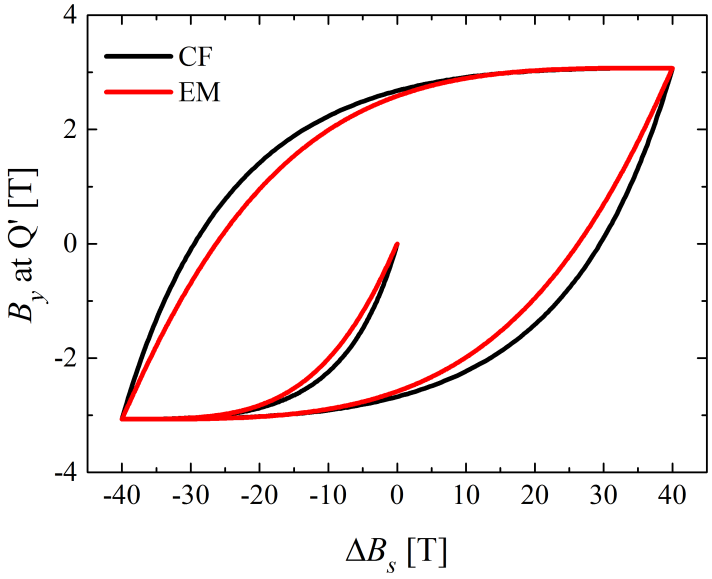

Figure 5.5: Dependence of B_y at Q' on ΔB_s by CF and EM method.

the bulk edge and the bulk center was much different, even in the bulk near the undulator center. Figure 5.7 shows the solenoid field dependence of undulator field by CF method (black) and EM method (red). The undulator field from EM method is much smaller than that from CF method at the same ΔB_s. The initial gradients of the curves, $\mathrm{d}B_0/\mathrm{d}\Delta B_s|_{\Delta B_s=0}$ of the EM and CF methods were 0.24 and 0.4, respectively, for all J_c^{bulk}.

5.3.3 Dependence on Thickness of Bulk HTS

Figure 5.8 shows the dependence of B_0 on the parameter f, which is defined by $f = 1 - D_z/\lambda_u$: the ratio of the horizontal gap between two bulk HTSs to the period. The numerical calculation was performed by the CF and EM methods with N = 12. To compare the numerical and analytical results, the numerical (analytical) fields at various f were normalized by the numerical (analytical) values for f = 0.5. In the analytical calculation and the numerical calculation by the CF method, for both $f < 0.5$ and

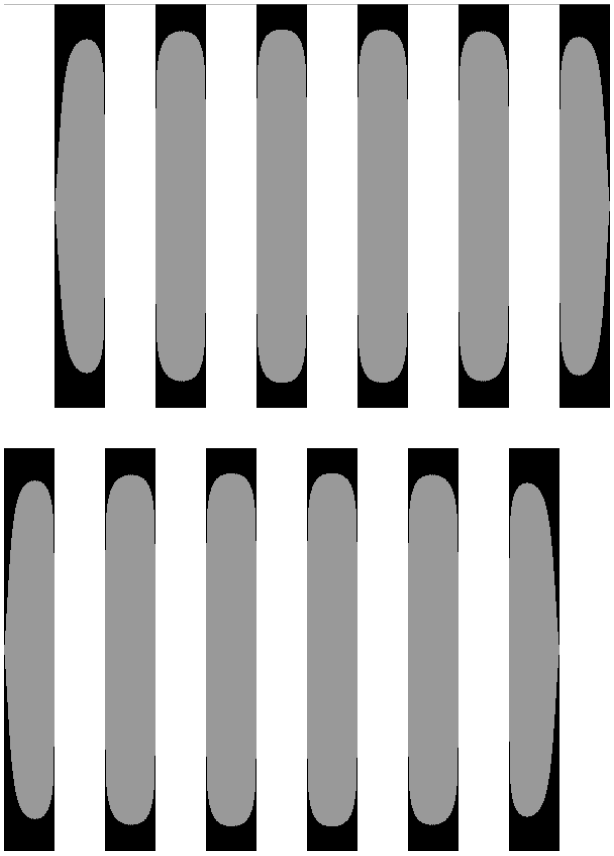

Figure 5.6: Cross sectional view of current distribution (x-direction current in zy plane) in BHSAU by EM method. The black and the gray areas indicate the regions in the bulk HTS in which the current flows and does not flow, respectively.

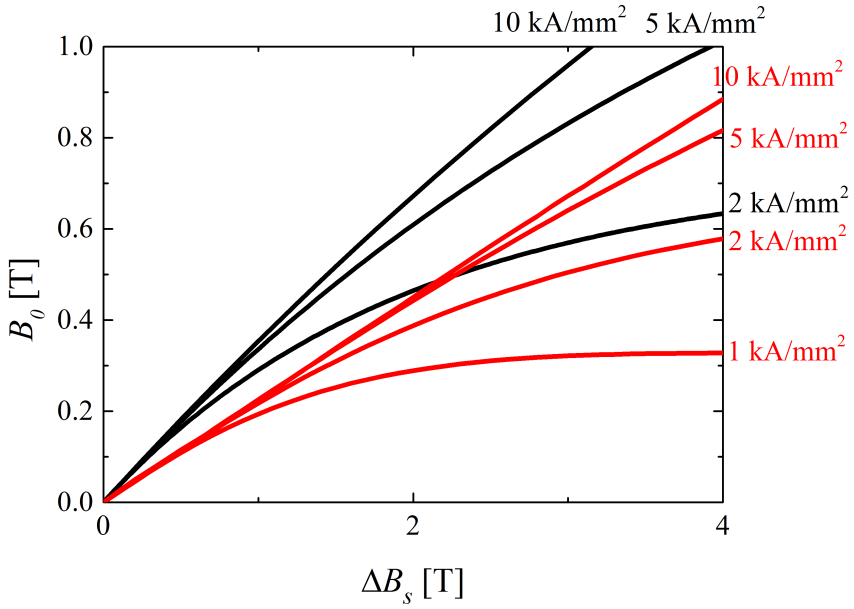

Figure 5.7: Solenoid field dependence of undulator field by CF method (black) and EM method (red).

$f > 0.5$ the almost same degradation of B_0 was observed for all ΔB_s. In contrast, in the numerical calculation by the EM method, the $f > 0.5$ condition sometimes resulted in a higher B_0 than the $f = 0.5$ condition at low ΔB_s.

5.4 Discussion

From the result of section 5.3.1, we found the following. Although the total current is almost the same for two methods, the current distribution is much different. In EM method, the depth of the current flowing layer at the both surface ($z = \pm D_z/2$) is much larger than that at the center ($z = 0$). This is because the more current is require to negate the field change at the surface. The current distribution in EM method is as expected. Thus, EM method looks more reasonable than CF method for single bulk HTS. However, the issue is not the difference of the current distribution, but the

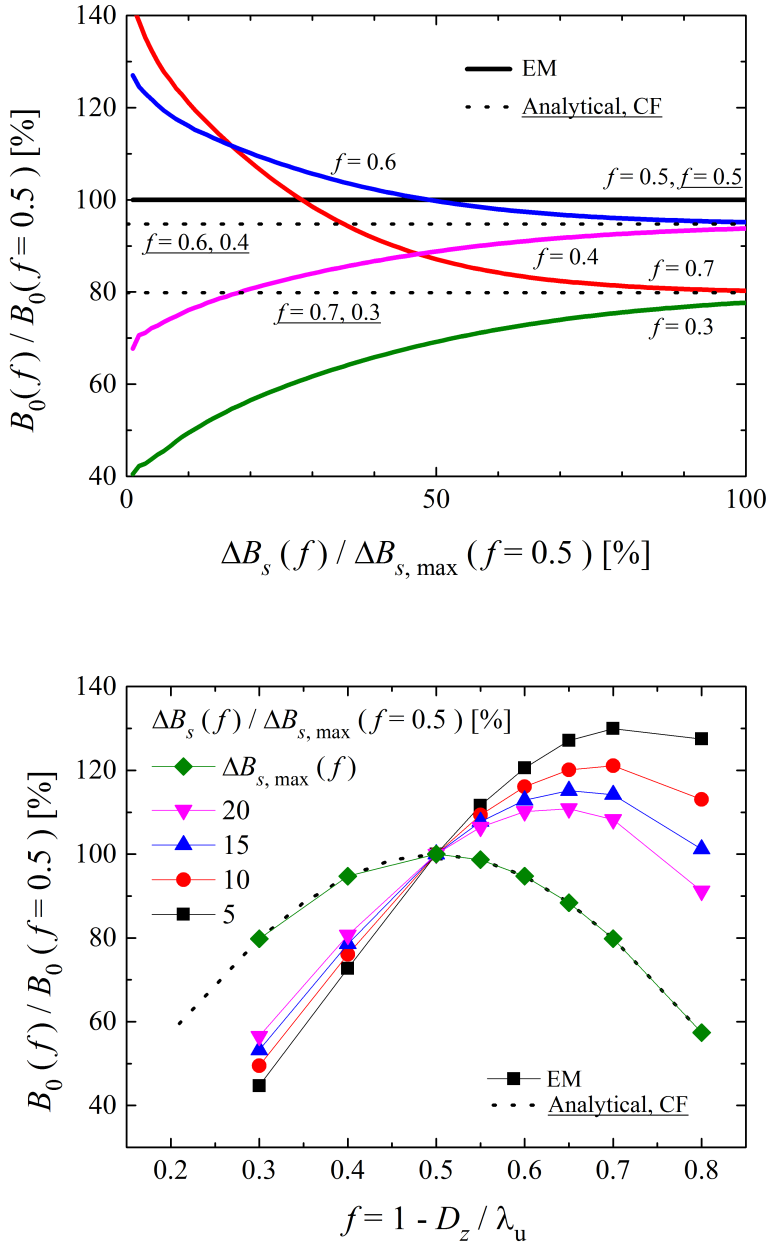

Figure 5.8: Dependence of B_0 on f (analytical, CF, and EM, g/λ_u = 0.4). For comparison, the analytical (numerical) fields at various f are normalized by the analytical (numerical) value for $f = 0.5$.

difference of B_y at Q'. This affects the undulator field.

From the result of section 5.3.2, we found that the depth of the current flowing layer at the bulk edge and the bulk center was much different, even in the bulk near the undulator center. As a consequence of that and small B_y mentioned above, the undulator field is found to be smaller than the expectation. This is directly shown. The total amounts of the current calculated by both methods were almost the same, however, the current distributions were much different. This is the reason of the difference in the undulator field amplitude.

From the result of section 5.3.3, we found a major difference in the dependences of B_0 on f by the calculation methods. As shown in Fig. 5.8, a higher B_0 was observed for $f > 0.5$ than when $f = 0.5$ for the same value of ΔB_s. Because the CF method and the analytical calculation did not exhibit this phenomenon, it is not due to the effect of the finite periodic number but to the current distribution inside the bulk HTSs shown in Fig. 5.6. Here we discuss this in detail. Currents with two different directions that are symmetric with respect to the z-axis generate equal value of B_y on z-axis with opposite signs. When $f < 0.5$, the numbers of such pairs increases with increasing bulk thickness; therefore, B_0 decreases. However, currents with two different directions that are symmetric with respect to a certain point on the z-axis generate the same B_y at the point. When $f > 0.5$, the numbers of such pairs decreases with decreasing bulk thickness; therefore, B_0 also decreases when $f > 0.5$ as with when $f < 0.5$. However, only in the EM method, there is an effect that increases B_0 when $f > 0.5$. In the EM method, the depth of the layer in which the current flows is large at the edge of the bulk. If the position of the edge moves in the z-direction to a point far from the field peak, the absolute field at the point decreases, although the B_y component increases in some cases. Therefore, in the EM method, B_0 increases or decreases depending on the current distribution at a certain ΔB_s when $f > 0.5$.

This dependence on f is opposite that for a conventional SAU, in which the undu-

lator field is high at $f < 0.5$ [29].

5.5 Conclusion

In this chapter, the effect of the current distribution in bulk HTSs on the undulator field of BHSAU is clarified. It was considered as the most important for the precise computation of the undulator field in BHSAU. To clarify the effect of the current distribution, the numerical result of center field method and the energy minimization method are compared. As a result, we found the following:

1. By introducing the current distribution into the calculation for single bulk, B_y at Q' was small

2. The depth of the current flowing layer at the bulk edge and the bulk center was much different, even in the bulk near the undulator center.

3. As a consequence of above two facts, the undulator field is found to has the difference from the expectation.

4. The undulator field can be large by selecting suitable ratio of the bulk thickness to the period.

Introduction of the current distribution bring us the precise undulator field calculation; and show the possibility of structure optimization which is impossible only with the theoretical study.

The future perspective of the numerical study of the BHSAU is as follows.

1. As a remained work of this thesis, the profile of B_y along the z-direction in the calculation by the CF and EM methods should be compared precisely. The undulator field may not a complete sinusoidal function of λ_u but the superposition of the harmonics. By comparing the high-harmonic components of the undulator

fields obtained by two methods, the effect of the current distribution on the field harmonics, which affect the radiation spectrum, may revealed.

2. One can use the numerical methods in this chapter to study the effect of the individual differences in the critical current densities of the bulk HTSs on the errors of the undulator field. Especially, the effect on the residual field integral and the phase error should be studied for the practical use of BHSAU. It is easy to introduce the different current densities to the bulk HTSs in the numerical code, and to calculate the errors numerically. The compensation methods for those errors can also be studied with that kind of numerical codes.

3. As a next step of the calculation by the EM method, one can introduce the dependence of J_c on the magnetic field (J_c–B relation) into the EM method. The methods to treating J_c–B relation has already established by Sanchez and Navau [42]. From the comparison of the results obtained by EM methods with and without J_c–B relation, the effect of that on the undulator field in the BHSAU may revealed.

4. The way to include the loop current which is not normal to z-axis should be considered. It may precisely calculate the field in the both ends of the undulator. However, because both the calculation by the CF and EM methods require the current path that are fixed in advance to the calculation, it is difficult to introduce such loop current into the calculation by those methods. The application of the full three-dimensional finite element methods for bulk HTSs to the calculation for the BHSAU is a candidate.

Chapter 6

Comparison of Experiment, Analytical-, and Numerical-Calculation

6.1 Introduction

In this chapter, we perform three studies by integrating the knowledge of the analysis, experiment, and numerical calculation. In section 6.2, the comparison of the calculation and the experiment is performed to validate the numerical model and reveal the average critical current density in the experiment. It is difficult to evaluate the agreement with absence of exact value of J_c. To solve the problem, the dependency curve of B_0 on ΔB_s is compared. The dependence curve in the experimental is compared with not only that in the EM method but also in the curve in the CF method to confirm the importance of the current distribution to reproduce the experiment. In section 6.3, the semi-empirical formula for the required solenoid field is derived by modifying the analytical formula using the results of the comparison between the analytical and numerical results with EM method. Though it is found in section 6.2 that

the EM method can precisely calculate the field inside BHSAU, it takes not small time and resources.The semi-empirical for the required solenoid field formula and the analytical formula of the undulator field can calculate the fields in the BHSAU including the factor of the current distribution inside the bulk HTSs. In section 6.4, the magnetic performance of BHSAU is estimated. To show how to use the formulae and values in tables, various example calculation is made.

6.2 Comparison between Experiment and Numerical Calculation

The experiment was performed with a 6-periodic-number, 10-mm-period, 4-mm-gap prototype with a 2 T superconducting solenoid and a helium gas cooling system. To equalize the geometry, the calculation was performed with a D-shape bulk with the same size as one used in the experiment, $f = 0.5$, $N = 6$, $\lambda_u = 10$ mm, and $g = 4$ mm. The experimental results have an error of 4% owing to the measurement error. The detailed setup of the experiment is described in Chapter 4. The detail of the numerical calculation is described in Chapter 5.

Figure 6.1 shows a comparison of the experimental and calculated solenoid field dependences of the undulator field. The experimental results show data obtained at T =20, 40, and 60 K. The calculation results show data obtained at J_c =10, 5, 2, and 1 kA/mm^2. The green dotted lines indicate the results obtained by the CF method. The pink solid lines indicate the results obtained by the EM method. The initial gradients of the curves, $\mathrm{d}B_0/\mathrm{d}\Delta B_s|_{\Delta B_s=0}$ of the experiment were 0.24 for all T, and those of the EM and CF methods were 0.24 and 0.4, respectively, for all J_c^{bulk}.

Figure 6.2 shows a comparison of the experimental and calculated field distributions of B_y along the z-axis. In the experiment, after the prototype was cooled to 20 K under a solenoid field of B_s = -2 T, the solenoid field was changed to B_s = 0 T ($\Delta B_s = +2$

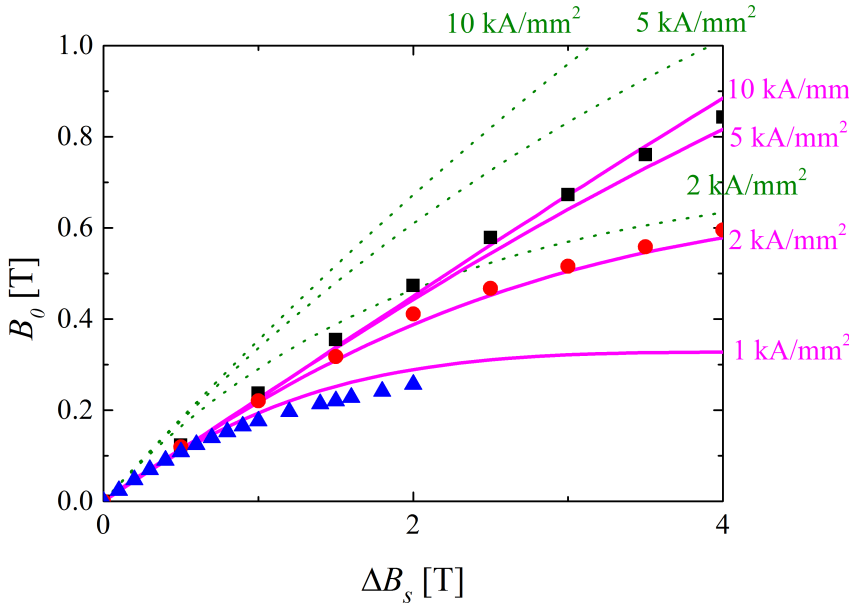

Figure 6.1: Comparison of the dependence of B_0 on ΔB_s in the experiment and calculation with CF method (green dotted line) and EM method (pink solid line)

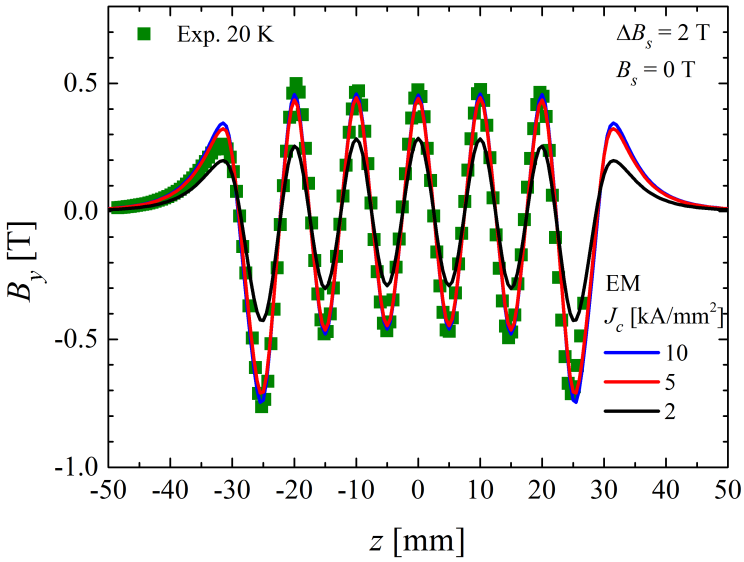

Figure 6.2: Comparison of B_y distribution along z-axis in the experiment and calculation with EM method.

T) at T = 20 K. This is known as field cooling. The calculation was performed by the EM method with J_c = 5 and 10 kA/mm^2.

6.2.1 Discussion

Here we evaluate the agreement between the calculation and experiment. It is difficult to compare the B_y profile or B_0 at a single value of ΔB_s without the exact value of the average J_c in the experiment. Thus, we used the dependence curve of B_0 on ΔB_s. As is clear from Formulae (3.32), and as shown in Fig. 3.7 in Chapter 2, the shape of the ΔB_s–B_0 curve and its initial gradient $\mathrm{d}B_0/\mathrm{d}\Delta B_s|_{\Delta B_s=0}$ do not depend on J_c but on the geometrical parameters. This was also true in the numerical calculation even when the depth of the layer in which the current flowed had a distribution in the z-direction inside the bulk, as shown in the numerical ΔB_s–B_0 curve in Fig. 5.7. The only excep-

tion is the case that the current distribution at each different T had a different shape for an equal $\Delta B_s/\Delta B_{s,\max}$. This is caused when the shape of the J_c–B curve changes markedly with T. However, we know from the DC magnetization measurement that the shape of the J_c–B curves did not show large shape change markedly with T and also this effect did not appear in the initial gradient of the experimental ΔB_s–B_0 curve in Fig. 6.1. Thus, by comparing the initial gradient, we can discuss the agreement without knowing the exact value of J_c.

From the comparison between the calculation and experiment, we clearly found that the results obtained by the EM method showed agreement with those of the experiment. The initial gradients of the curves in the experiment and the EM method are identical, whereas the initial gradient in the CF method is 1.7 times larger than that in the experiment. Moreover, the dependence curve of B_0 on ΔB_s in the calculation by the EM method is similar to that in the experiment. From the comparison, we can estimate the range of the average J_c in the experiment. Because the average J_c changes with the field, it is difficult and meaningless to estimate the exact value to fit the curve. The estimated average ranges of J_c were 5 - 10 kA/mm^2 at T = 20 K, 2–3 kA/mm^2 at T = 40 K, and approximately 1 kA/mm^2 at T = 60 K. These ranges are almost within the ranges from $J_c(B = 0)$ to $J_c(B = 2\ \mathrm{T})$ in Table 4.2, and are thus thought to be reasonable. From these findings, we can conclude that the results of the EM method show agreement with those of the experiment. Additionally, we found that the macroscopic J_c in the bulk HTSs was almost equal to that of the small sample. This means that the large degradation due to the difficulty of manufacturing large bulk HTSs or cracking did not occur.

The reason for the agreement is next discussed. The geometrical parameters N, λ_u, g, D_x, D_y, and D_z and the bulk shape were equal in the experiment, the CF method, and the EM method. As stated in Section III.A, the total amounts of the current inside the bulk at the same ΔB_s are only slightly different for the two calculation methods.

The only remaining factor is the geometrical shape of the current, i.e. the current distribution inside the bulk. Therefore, we conclude the following. The reason why the EM method closely reproduced the experiment is that it closely reproduced the current distribution in the experiment. The current distribution inside the bulk must be considered to precisely estimate the field inside the BHSAU,

We next discuss the results shown in Fig. 6.2. On the basis of above discussion, the calculation was performed by the EM method with $J_c = 5$ and 10 kA/mm^2. The difference between the results obtained experimentally and by calculation for both J_c is less than 5% except near the peak at $z \sim -32$ mm. By considering the fact that the measurement has an error of 4%, the difference of 5% is not large. The difference near the peak at $z \sim -32$ mm is about 30%. There are two possible reasons for this large difference. One is that the individual differences in J_c among the bulk HTSs particularly affects peaks near the ends of the undulator. The other is that the current distribution cannot be reproduced well near the ends of the undulator even by the EM method when the magnetization is not perpendicular to the xy-plane. The former effect can be included in the calculation by including the individual differences in J_c among the bulk HTSs. For the latter case, it is difficult to measure the actual current distribution inside the bulk HTSs. However, the difference can be evaluated by comparing a much larger amount of data, i.e., the B_y and B_z distributions in three-dimensional space near the ends of the undulator. If a difference appears, the assumption that the current flows only in the plane perpendicular to the z-axis should be changed in a future calculation.

Although the amplitude of the undulator field can be obtained by the empirical formulae derived in the next section, the numerical code remains useful in the future study. As PMs have the individual difference in magnetization, bulk HTSs also have that in critical current density, which cause the errors in the undulator field, so called phase error and residual field integrals. The compensation methods for these errors are

the practically important and the next topic of our study. It is not difficult to modify the numerical code to treat the individual difference in the critical current density of bulk HTS. Therefore, the numerical code can be used to study the compensating methods for these errors.

6.3 Semi-Empirical Formula

6.3.1 Comparison between Analytical and Numerical Calculations

Figure 6.3 shows the difference in the analytical and numerical values of ΔB_s required for the same B_0. Here, the superscripts An and Nu indicate analytical and numerical values, respectively. The numerical calculation was performed by the EM method with N = 12. B_0^{An} and ΔB_s^{An} are the values obtained by Formulae (3.16) and (3.17) in Chap. 3. In the numerical calculation, a larger ΔB_s than the analytical value was required to generate the same B_0, particularly for low B_0. For $f = 0.5$, the numerical value of ΔB_s required was up to 50% higher than the analytical value. For $f > 0.5$, the requirement was moderate at low B_0. The divergence at high B_0 for $f > 0.5$ means that $B_0(f)$ ($f > 0.5$) cannot reach to $B_{0,\max}$ ($f = 0.5$).

6.3.2 Semi-Empirical Formula for Required Solenoid Field

Here we modify the analytical formulae by using the results obtained by comparing the numerical and analytical calculations. The maximum B_0 in the numerical calculation is equal to that in the analytical calculation; therefore, the target range of the modification is the *reasonable operation range* discussed above, and modification should be applied to the formula for ΔB_s but not to the formula for B_0:

$$B_0^{\mathrm{Nu}} = B_0^{\mathrm{An}}, \tag{6.1}$$

$$\Delta B_s^{\mathrm{Nu}} = (1 + \alpha)\, \Delta B_s^{\mathrm{An}}. \tag{6.2}$$

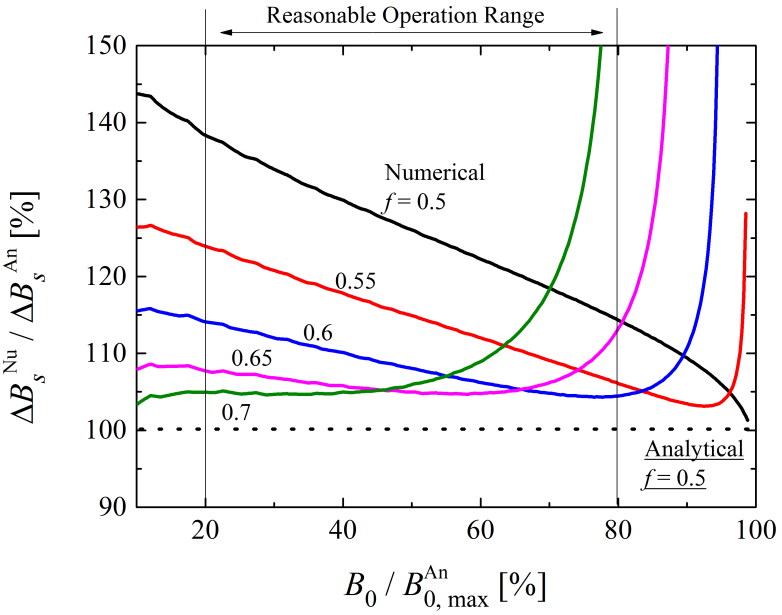

Figure 6.3: Difference in the analytical and numerical values of ΔB_s required for the same B_0 (analytical and EM, $g/\lambda_u = 0.4$). The superscripts An and Nu indicate analytical and numerical values, respectively. The numerical calculation was performed by the EM method with $N = 12$.

Table 6.1: Parameters for Formula (6.3)

	$a + bx + c\exp(dx)$				effective range
f	a	b	c	d	$B_0/B_{0,\max}$ [%]
0.55	0.296	-0.294	-	-	20–90
0.60	0.176	-0.188	7.93 $\times 10^{-9}$	18.2	20–90
0.65	0.0995	-0.107	1.50 $\times 10^{-5}$	11.2	20–80
0.70	0.0551	-0.0346	1.47 $\times 10^{-4}$	9.89	20–70

As shown in Fig. 6.3, the factor α is at most 50%. However, if a suitable f is chosen for the target operation point, it can be less than 5%. We fit the curves by the empirical formula

$$\alpha = a + b\frac{B_0^{\mathrm{An}}}{B_{0,\max}^{\mathrm{An}}} + c\exp\left(d\frac{B_0^{\mathrm{An}}}{B_{0,\max}^{\mathrm{An}}}\right). \tag{6.3}$$

$$(\text{for } a,\ b,\ c,\ \text{and } d,\ \text{see Table 6.1})$$

The fitting results of the parameters $a,\ b,\ c$, and d are shown in Table 6.1. The error of the formula is less than 1% in the effective range shown in Table 6.1.

Additionally, we consider the effect of the periodic number. Because we used $N = 12$ in the calculation for Fig. 6.3, the required ΔB_s should be modified as

$$\Delta B_s^{\mathrm{Nu}}(N) = \beta(N) \times (1+\alpha)\,\Delta B_s^{\mathrm{An}}. \tag{6.4}$$

Here, β is a function of the periodic number, and the right term of the multiplication is the value when $N = 12$. By fitting the dependence curve of ΔB_s on N for $B_0/B_{0,\max} = 50\%$, we have

$$\beta(N) = 1.098 - 1.060\frac{1}{N} - 1.519\frac{1}{N^2}. \tag{6.5}$$

The error of this formula is less than 1% in the range of $6 \le N$ and $20 \le B_0/B_{0,\max} \le 90$.

Formula (6.4) reproduces the numerical B_0 and ΔB_s with an error of less than 2% for $D_y = \lambda_u/2$, $g/\lambda_u = 0.4$, $6 \leq N$, and the effective $B_0/B_{0,\max}$ range shown in Table 6.1. Moreover, because it is clear from Table 3.2 that the shape of the ΔB_s–B_0 curve has a difference of less than 2% among various values of g/λ_u, this modified formula can be applied to a wide range of conditions ($0.1 \leq g/\lambda_u \leq 10$) with an error of less than 3%.

6.3.3 Performance Estimation of BHSAU

Here we estimate the magnetic performance of the BHSAU as an example of using the formulae and the values obtained above. As examples of performance estimation, we calculated two patterns with λ_u = 18 mm and g = 3.6 mm by targeting a twice as large field as that generated in the IVU but with an equal period and gap. Next, we calculated two patterns with λ_u = 10 mm and g = 4 mm by targeting K = 2 and two patterns with λ_u = 5 mm and g = 1 mm by targeting K = 1 and 2. Here, K is called the diffraction parameter and is defined by $K = eB_0\lambda_u/(2\pi mc)$, where e and m are the electron charge and mass, respectively. To obtain bright undulator radiation, $K \sim$ 1–2 is required.

In Table 6.2, we show estimated B_0, and the values of ΔB_s and the operation temperature T required to obtain each B_0. Here, ΔB_s is the value for N = 50. Note that Γ_y is not the actual depth of the layer in which the current flows and is simply the index in Table 3.2. We set $J_c^{\rm bulk}$, Γ_y, f, and T to meet the following conditions: (i) $\Delta B_s/2$ does not exceed 6 T, (ii) J_c^{bulk} is in the range from $J_c(B = 0)$ to $J_c(B = \Delta B_s/2)$ at T, (iii) f is chosen to obtain a small α. Here, we assumed the field cooling method, i.e., the undulator is cooled to below the superconducting transition temperature under a solenoid field of $-\Delta B_s/2$ and operated under a solenoid field of $\Delta B_s/2$. Thus, we used J_c^{bulk} in the range between $J_c(B = 0)$ and $J_c(B = \Delta B_s/2)$.

As shown in the table, an undulator field twice as large as that of the present IVU

Table 6.2: Performances of BHSAU

λ_u [mm]	g [mm]	J_c^{bulk} [kA/mm^2]	Γ_y [%]	f	B_0 [T]	$\Delta B_s/2$ [T]	T [K]	K
18	3.6	2.4	30	0.6	2.6	4.8	40	4.4
		7.1	5	0.7	2.6	2.3	20	4.4
10	4	8.0	20	0.6	2.1	6.0	20	2.0
		12.0	10	0.65	2.1	4.4	10	2.0
5	1	7.1	30	0.6	2.1	3.9	20	1.0
		16.7	20	0.6	4.2	6.0	4	2.0

but with an equal period and gap can be obtained at temperatures of approximately 20–40 K. Moreover, K = 1 or 2 can be achieved with a short period such as 5 or 10 mm. Because B_0 of over 4 T is required to achieve K = 2 at λ_u = 5 mm, it is impossible to achieve this using PM undulators even with g = 0. Although $T = 4$ K is required to achieve the condition of the bottom row in Table 6.2 with currently available bulk HTSs, if the critical current density of the bulk HTS is doubled as a result of future material developments, the BHSAU can be operated at approximately 20 K. We believe that the magnetic field strength of the BHSAU is sufficiently high for future high-field short-period undulators.

Chapter 7

Summary

This thesis discusses the characteristics of BHSAU aiming at the realization of the short-period high-field undulator using the bulk high-temperature superconductor.

The results are summarized as follows.

1. The analytical formulae of the field inside the BHSAU was derived from the model based on the two-dimensional approximation and Bean's critical state model for hard type-II superconductor, by using the two-dimensional Biot-Savart's law. The analytical calculation revealed the field profile inside BHSAU and their degree of dependence on the geometrical parameters, the critical current density of the bulks, and the solenoid field. The calculation showed that the theoretical maximum of the undulator field of the BHSAU is much higher than that of the conventional undulators and that the undulator field amplitude can be controlled by the solenoid field in the wide range.

2. The prototype experiment was performed in the small 6-period prototype with the 2-T superconducting solenoid and the helium gas cooling system. The sinusoidal magnetic field, i.e. the undulator field, was generated successfully. The amplitude of the undulator field was well controlled by the solenoid field. The

undulator field of 0.85 T was achieved. This value is higher than that of the present permanent magnet undulators. Further increment of the undulator field with a strong solenoid can be expectable from the curve of the undulator field dependence on the solenoid field.

3. The three-dimensional numerical model of BHSAU was created. The numerical calculation was performed with CF and EM methods. From the comparison of the results by two methods which derive the different current distribution, we found that the undulator fields by two methods are much different whereas the amounts of the currents inside bulk HTSs are almost the same. We also found additional characteristics of BHSAU by the EM method which is not found in the analytical calculation; the undulator field can be increased several tens percent under the equal solenoid field by using the bulk thinner than the half of the period.

4. Comparison between the calculation and experiment was made. The numerical results with the EM method show good agreement with the experiment. We found that the current distribution is important to estimate precise undulator field inside BHSAU. Comparison between the analytical and numerical calculation are performed. By using the result of that, we proposed a semi-empirical formula of the solenoid field by modifying the analytical formulae to include the factor of the current distribution. The formulae, i.e., the analytical formula of the undulator field and the semi-empirical formula of the solenoid field, can calculate the fields in the BHSAU with the difference of within 3% from the numerical results without large time and hardware resources for the calculation. We showed the various magnetic performance estimation of BHSAU using the formulae and the values obtained in this thesis. The estimation showed that the undulator field of the BHSAU at approximately 20-40 K was twice as large as that of IVU but with the same period and gap (IVU in SACLA, the period of 18 mm and the gap of 3.6 mm). Also the estimation showed the possibility of the realization of a short-

period, high-field undulator by the BHSAU. The diffraction parameter (K value) of 1 and 2 can be achievable at approximately 20-40 K with 6-T solenoid and 10-mm-period and 4-mm-gap. The diffraction parameter (K value) of 1 and 2 can be achievable at approximately 4-20 K with 6-T solenoid and 5-mm-period and 1-mm-gap.

In summary, the characteristics of BHSAU were studied in the analytical, numerical, and experimental ways. The practical strength undulator field generation was demonstrated.

The future perspective of the study is as follows. For the undulator field, not only the field strength but also the quality of the field is important to obtain the high quality undulator radiation. The most important work in future is increasing the measurement accuracy of the magnetic field inside BHSAU under the condition of very narrow gap, low temperature, and in-vacuum. With the precise magnetic field over the wide ranges of the undulator field and the solenoid field, the trajectory of the electron beam and the spectrum of the radiation from it can be calculated, and, if the need arises, the compensation methods of them can be investigated. The numerical model of BHSAU also can be discussed at the more precise level. Then, the compensation methods for field quality can be discussed by using the numerical code. Another important work is investigating the method to keep the undulator field constant under the flux creep phenomenon. The methods mentioned in chapter 4 should be studied.

Appendix A

Integration for Magnetic Field

Let us integrate the equation:

$$b^*(\xi) = -\frac{\mu_0}{2\pi \mathrm{i}} \frac{I}{\lambda_u} \int_{-\infty}^{\infty} \frac{1 + 2\sum_{n=1}^{\infty} \cos \beta z'}{z' - \xi} \mathrm{d}z'. \tag{A.1}$$

Here, $\xi = z + \mathrm{i}y$ and $\beta = 2n\pi/\lambda_u$. Executing the integration for the first term, we have

$$PV \int_{-\infty}^{\infty} \frac{1}{z' - \xi} \mathrm{d}z' = \begin{cases} +\mathrm{i}\pi & (\Im(\xi) > 0), \\ -\mathrm{i}\pi & (\Im(\xi) < 0). \end{cases} \tag{A.2}$$

Here, we adopt Cauchy's principal value and $\Im(\xi)$ is the imaginary part of ξ.

To execute the integration for the second term, let us think the integration paths in Fig. A.1. Here, $\mathrm{C_u}$ and $\mathrm{C_l}$ are the loop path around the upper and lower semi-circle with the radius R, respectively. $\mathrm{S_u}$ and $\mathrm{S_u}$ are only the arc of those. Note that cosine

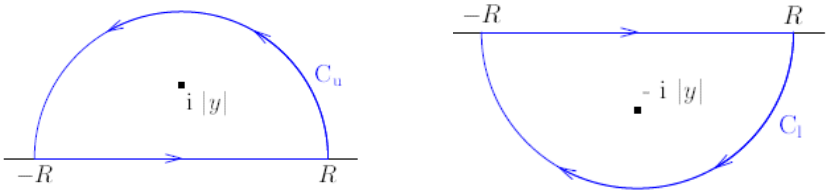

Figure A.1: Upper (LEFT) and lower (RIGHT) integration path

function has essential singularity at infinite distance. Then, we have

$$\begin{aligned}\int_{-\infty}^{\infty}\frac{\cos(\beta z')}{z'-\xi}\mathrm{d}z' &= \frac{1}{2}\int_{-\infty}^{\infty}\frac{e^{\mathrm{i}\beta z'}+e^{-\mathrm{i}\beta z'}}{z'-\xi}\mathrm{d}z' \\ &= \frac{1}{2}\lim_{R\to\infty}\left[\left(\oint_{\mathrm{C_u}}-\int_{\mathrm{S_u}}\right)\frac{e^{\mathrm{i}\beta\zeta}}{\zeta-\xi}\mathrm{d}\zeta+\left(\oint_{\mathrm{C_l}}-\int_{\mathrm{S_l}}\right)\frac{e^{-\mathrm{i}\beta\zeta}}{\zeta-\xi}\mathrm{d}\zeta\right] \\ &= \begin{cases}+\pi\mathrm{i}\left[\mathrm{Res}(e^{+\mathrm{i}\beta\zeta},\xi)\right] & (\Im(\xi)>0),\\ -\pi\mathrm{i}\left[\mathrm{Res}(e^{-\mathrm{i}\beta\zeta},\xi)\right] & (\Im(\xi)<0).\end{cases}\end{aligned} \tag{A.3}$$

Here, $\mathrm{Res}(e^{+\mathrm{i}\beta\zeta},\xi)$ is the residue of the $e^{+\mathrm{i}\beta\zeta}\,\mathrm{d}\zeta$ at $\zeta=\xi$. The integration along $\mathrm{S_u}$ and $\mathrm{S_l}$ are vanished at $R\to\infty$.

As a result, we obtain

$$b_z = \mathrm{sgn}(y)\frac{\mu_0 I}{2\lambda_u}\left[1+2\sum_{n=1}^{\infty}\cos(\beta z)e^{-\beta|y|}\right], \tag{A.4}$$

$$b_y = -\frac{\mu_0 I}{\lambda_u}\sin(\beta z)e^{\beta|y|}. \tag{A.5}$$

Acknowledgments

I would like to thank Prof. Kai Masuda of Kyoto University for supervision of my research.

I would like to thank Prof. Hideaki Ohgaki and Prof. Kazunobu Nagasaki of Kyoto University for their meaningful comments.

I would like to thank members of Nagasaki and Ohgaki Laboratory in Kyoto University, Prof. Kii for consulting budgets, Dr. Zen for discussion on results, Dr. Ohshima for helpful comments, Mr. Mishima and Mr. Imon for supporting experiments, and Mr. Hada for studying numerical methods together. I would also like to thank all students and staffs in Uji campus who helped and encouraged my research life in doctor course.

I appreciate Dr. T. Teshima and Dr. M. Morita of Nippon Steel Corporation for providing QMG-GdBCO and useful information. I also appreciate members in Niki Glass Co., Ltd. for their persevering contribution on the experimental system. The DC magnetization of small QMG-GdBCO were measured and analyzed with the help of Prof. M. Azuma at Institute of Chemical Research, Kyoto University (at that time).

I would like to thank Dr. Takashi Tanaka and my colleagues at SPring-8. Without their understandings, I could not finish my thesis.

This work was supported by MEXT KAKENHI Grant Number 21340057 and a Grant-in-Aid for JSPS Fellows, Grant Number 10J03477, also partially supported by MEXT KAKENHI Grant Number 17684009 and Global COE program of Kyoto University “toward CO2 Zero-emission Energy System.”

Bibliography

[1] P. M. Stefan, T. Tanabe, S. Krinsky, G. Rakowsky, L. Solomon, and H. Kitamura. Initial results from an in-vacuum undulator in the NSLS x-ray ring. *J. Synchrotron Radiat.*, 5:417, 1997.

[2] T. Schmidt, G. Ingold, A. Imhof, B. D. Patterson, L. Patthey, C. Quitmann, C. Schulze-Briese, and R. Abela. Inserion device at the swiss light source (phase i). *Nucl. Instrum. Methods Phys. Res., Sect. A*, 467:126, 2001.

[3] J. A. Clarke. Possible insertion devices for the diamond light source. In *Proc. European Particle Accelerator Conf. 2010*, page 2319, Vienna, Austria, 2010.

[4] O. Chubar, C Benabderrahmane, M. P. Level, O. Marcouille, and M. Massal. Soleil insertion devices: The progress report. In *Proc. European Particle Accelerator Conf. 2004*, page 369, Lucerne, Switzerland, 2004.

[5] P. Emma, R. Akre, J. Arthur, R. Bionta, C. Bostedt, J. Bozek, A. Brachmann, P. Bucksbaum, R. Coffee, F. J. Decker, Y. Ding, D. Dowell, S. Edstrom, A. Fisher, J. Frisch, S. Gilevich, J. Hastings, G. Hays, Ph. Hering, Z. Huang, R. Iverson, H. Loos, M. Messerschmidt, A. Miahnahri, S. Moeller, H.D. Nuhn, G. Pile, D. Ratner, J. Rzepiela, D. Schultz, T. Smith, P. Stefan, H. Tompkins, J. Turner, J. Welch, W. White, J. Wu, G. Yocky, and J. Galayda. First lasing and operation of an ångstrom-wavelength free-electron laser. *Nat. Photonics*, 4:641, 2010.

[6] M. Hoener, L. Fang, O. Kornilov, O. Gessner, S. T. Pratt, M. Gühr, E. P. Kanter, C. Blaga, C. Bostedt, J. D. Bozek, P. H. Bucksbaum, C. Buth, M. Chen, R. Coffee, J. Cryan, L. DiMauro, M. Glownia, E. Hosler, E. Kukk, S. R. Leone, B. McFarland, M. Messerschmidt, B. Murphy, V. Petrovic, D. Rolles, and N. Berrah. Ultraintense x-ray induced ionization, dissociation, and frustrated absorption in molecular nitrogen. *Phys. Rev. Lett.*, 104:253002, Jun 2010.

[7] T. Ishikawa, H. Aoyagi, T. Asaka, Y. Asano, N. Azumi, T. Bizen, H. Ego, K. Fukami, T. Fukui, Y. Furukawa, S. Goto, H. Hanaki, T. Hara, T. Hasegawa, T. Hatsui, A. Higashiya, T. Hirono, N. Hosoda, M. Ishii, T. Inagaki, Y. Inubushi, T. Itoga, Y. Joti, M. Kago, T. Kameshima, H. Kimura, Y. Kirihara, A. Kiyomichi, T. Kobayashi, C. Kondo, T. Kudo, H. Maesaka, X. M. Marechal, T. Masuda, S. Matsubara, T. Matsumoto, T. Matsushita, S. Matsui, M. Nagasono, N. Nariyama, H. Ohashi, T. Ohata, T. Ohshima, S. Ono, Y. Otake, C. Saji, T. Sakurai, T. Sato, K. Sawada, T. Seike, K. Shirasawa, T. Sugimoto, S. Suzuki, S. Takahashi, H. Takebe, K. Takeshita, K. Tamasaku, H. Tanaka, R. Tanaka, T. Tanaka, T. Togashi, K. Togawa, A. Tokuhisa, H. Tomizawa, K. Tono, S. Wu, M. Yabashi, M. Yamaga, A. Yamashita, K. Yanagida, C. Zhang, T. Shintake, H. Kitamura, and N. Kumagai. A compact x-ray free-electron laser emitting in the sub-angstrom region. *Nat. Photonics*, 6:540, 2012.

[8] J. Dai, H. Deng, and Z. Dai. Proposal for an x-ray free electron laser oscillator with intermediate energy electron beam. *Phys. Rev. Lett.*, 108:034802, Jan 2012.

[9] D. J. Scott, J. A. Clarke, D. E. Baynham, V. Bayliss, T. Bradshaw, G. Burton, A. Brummitt, S. Carr, A. Lintern, J. Rochford, O. Taylor, and Y. Ivanyushenkov. Demonstration of a high-field short-period superconducting helical undulator suitable for future tev-scale linear collider positron sources. *Phys. Rev. Lett.*, 107:174803, Oct 2011.

[10] H. Kitamura. Recent trends of insertino-device technology for x-ray sources. *J. Synchrotron Radiat.*, 7:121, 2000.

[11] T. Hara, T. Tanaka, H. Kitamura, T. Bizen, X. Maréchal, T. Seike, T. Kohda, and Y. Matsuura. Cryogenic permanent magnet undulators. *Phys. Rev. ST Accel. Beams*, 7:050702, May 2004.

[12] T. Hezel, B. Krevet, H. O. Moser, J. A. Rossmanith, R. Rossmanith, and T. Schneider. A superconductive undulator with a period length of 3.8 mm. *J. Synchrotron Radiat.*, 5:448, 1998.

[13] M. Tomita and M. Murakami. High-temperature superconductor bulk magnets that can trap magnetic fields of over 17 tesla at 29 k. *Nature*, 421:517, 2003.

[14] T. Tanaka, T. Hara, H. Kitamura, R. Tsuru, T. Bizen, X. Marechal, and T. Seike. Application of high-temperature superconducting permanent magnets to synchrotron radiation source. *Phys. Rev. ST Accel. Beams*, 7:090704, 2004.

[15] T. Tanaka, R. Tsuru, and H. Kitamura. analytical formula, offset elimination, 1.5 t. *J. Synchrotron Radiat.*, 12:442, 2005.

[16] T. Tanaka, T. Hara, R. Tsuru, D. Iwaki, T. Bizen, X. Marechal, T. Seike, and H. Kitamura. Utilization of bulk high-temperature suerpconductors for shorter-period synchrotron radiation sources. *Supercond. Sci. Technol.*, 19:S438, 2006.

[17] R. Kinjo, T. Kii, H. Zen, K. Higashimura, K. Masuda, K. Nagasaki, and H. Ohgaki. A bulk high-tc superconductor staggered array undulator. In *Proc. 30th Int. Free Electron Laser Conf.*, page 473, Geongju, Korea, 2008.

[18] A. H. Ho, R. H. Pantell, J. Feinstein, and B. Tice. A novel wiggler design for use in a high-efficiency free-electron laser. *Nucl. Instrum. Methods Phys. Res., Sect. A*, 296:631, 1990.

[19] C. P. Bean. Magnetization of high-field superconductors. *Rev. Mod. Phys.*, 36:31, 1964.

[20] J. Kitagaki. *Design Study of the Staggered Array Undulator for Free Electron Lasers*. PhD thesis, Kyoto University, 2000.

[21] C. A. Brau. *Free Electron Lasers*. Academic Press, Inc., 1990.

[22] Y. B. Kim, C. F. Hempstead, and A. R. Strnad. Critical persistent currents in hard superconductors. *Phys. Rev. Lett.*, 9:306–309, 1962.

[23] F. Irie and K. Yamafuji. Theory of flux motion in non-ideal type-ii superconductor. *J. Phys. Soc. Jpn.*, 23:255–268, 1967.

[24] R. Kinjo, T. Kii, M. A. Bakr, K. Higashimura, K. Yoshida, S. Ueda, T. Sonobe, K. Masuda, K. Nagasaki, and H. Ohgaki. Variation of undulator field in bulk htsc staggered array undulator. In *Proc. Particle Accelerator Society Meeting 2009*, pages 344–346, JAEA, Tokai, Japan, 2009.

[25] H. Motz. Applications of the radiation from fast electron beams. *J. Appl. Phys.*, 22:527, 1951.

[26] L. R. Elias, W. M. Fairbank, J. M. L. Madey, H. A. Schwettman, and T. I. Smith. Observation of stimulated emission of radiation by relativistic electrons in a spatially periodic transverse magnetic field. *Phys. Rev. Lett.*, 36:717, 1976.

[27] M. Bazin, Y. Farge, M. Lemonnier, J. Pero, and Y. Petroff. Design of an undulator for a.c.o. and its possible use as free electron laser. *Nucl. Instrum. Meth.*, 172:61, 1980.

[28] H. Winick, G. Brown, K. Halbach, and J. Harris. Wiggler and undulator magnets. *Physics Today*, 34:50, 1981.

[29] J. Kitagaki, K. Masuda, Z. W. Dong, T. Kii, T. Yamazaki, and K. Yoshikawa. A design study on electron beam confinement in a staggered array undulator based on a 3d code. *Nucl. Instrum. Methods Phys. Res., Sect. A*, 475:613–616, 2001.

[30] T. Kii. Mext kakenhi grant number 17684009, 2005–2007.

[31] N. Okawachi M. Nakano K. Masuda H. Ohgaki K. Kyoshikawa T. Yamazaki T. Kii, H. Zen. Design study on high-tc superconducting micro-undulator. In *Proc. 28th Int. Free Electron Laser Conf.*, pages 653–655, 2006.

[32] M. Morita, E. Teshima, and H. Hirano. Development of oxide superconductors - high-Tc bulk superconductor, QMG, and its magnetic applications. Technical report, Nippon Steel Corporation, 2006.

[33] F. Yeh and K. W. White. Fracture toughness behavior of the $YBa_2Cu_3O_{7-x}$ superconducting ceramic with silver oxide additions. *J. Appl. Phys.*, 70:4989–4994, 1991.

[34] G. Fuches and. Trapped magnetic field larger than 14 T in bulk $YBa_2Cu_3O_{7-x}$. *Appl. Phys. Lett.*, 76:2107–2109, 2000.

[35] M. Morita et al. Trapped field and mechanical properties of QMG magnet. In *Proc. 1998 Int. Workshop on Superconductivity*, pages 115–118, ISTEC, Tokyo, Japan, 1998.

[36] M. Tomita and M. Murakami. Improvement of the mechanical properties of bulk superconductors with resin impregnation. *Supercond. Sci. Technol.*, 13:722–724, 2000.

[37] J. Z. Sun, B. Lairson, C. B. Eom, J. Bravman, and T. H. Geballe. Elimination of current dissipation in high transition temperature superconductors. *Science*, 247:307, 1990.

[38] T. Kii, R. Kinjo, M. A. Bakr, Y. W. Choi, K. Yoshida, S. Ueda, M. Takasaki, K. Ishida, N. Kimura, T. Sonobe, K. Masuda, and H. Ohgaki. A study on field error of bulk htsc staggered array undulator originated from variation of critical current density of bulk htscs. In *Proc. 32th Int. Free Electron Laser Conf.*, page 648, Malmo, Sweden, 2010.

[39] T. Kii, R. Kinjo, N. Kimura, M. Shibata, M. A. Bakr, Y. W. Choi, M. Omer, K. Yoshida, K. Ishida, T. Komai, K. Shimahashi, T. Sonobe, H. Zen, K. Masuda, and H. Ohgaki. Low-temperature operation of a bulk htsc staggered array undulator. *IEEE Trans. Appl. Supercond.*, 22:4100904, 2012.

[40] O. Chubar, P. Elleaume, and J. Chavanne. A three-dimensional magnetostatics computer code for insertion devices. *J. Synchrotron Radiat.*, 5:481–484, 1998.

[41] A. Badía, C. López, and J. L. Giordano. Optimal control model for the critical state in superconductors. *Phys. Rev. B*, 58:9440–9449, 1998.

[42] A. Sanchez and C. Navau. Magnetic properties of finite superconducting cylinders. I. Uniform applied field. *Phys. Rev. B*, 64:214506, 2001.

List of Publication

Chapter 2

[1] R. Kinjo, K. Higashimura, T. Kii, H. Zen, K. Masuda, K. Nagasaki, H. Ohgaki and Y. U. Jeong, "A Bulk High-Tc Superconductor Staggered Array Undulator", *Proceedings of the 30th International Free Electron Laser Conference 2008*, May 5, 2009.

Chapter 5

[2] R. Kinjo, T. Kii, M. A. Bakr, K. Higashimura, K. Yoshida, S. Ueda, K. Masuda, K. Nagasaki, H. Ohgaki, T. Sonobe and H. Zen, "Numerical Evaluation of Bulk HTSC Staggered Array Undulator by Bean Model", *Proceedings of the 31th International Free Electron Laser Conference 2009*, Dec. 17, 2009.

Chapter 2, 5

[3] T. Kii and R. Kinjo, "Application of Bulk High-temperature Superconductor to Insertion Device for Synchrotron Radiation", *TEION KOUGAKU (in Japanese)*, Vol. 46 (2011) 118 (refereed).

Chapter 4

[4] R. Kinjo, M. Shibata, T. Kii, H. Zen, K. Masuda, K. Nagasaki and H. Ohgaki, "Demonstration of a High-Field Short-Period Undulator Using Bulk High-Temperature Superconductor", *Applied Physics Express*, Vol. 6 (2013) 042701 (refereed).

Chapter 3, 4, and 6

[5] R. Kinjo, K. Mishima, M. Omer, Y. W. Choi, K. Yoshida, H. Negm, H. Imon, M. Shibata, K. Shimahashi, K. Okumura, M. Inukai, H. Zen, T. Kii, K. Masuda, K. Nagasaki and H. Ohgaki, "Magnetic Properties of Staggered-Array Undulator Using Bulk High-Temperature Superconductor", *Physical Review Special Topics - Accelerators and Beams*, Vol. 17 (2014) 022401 (refereed).

The contents in these chapters are from R.Kinjo et al., Phys. Rev. ST Accel. Beams, 17 (2014) 022401, Copyright (2014) of American Physical Society.

Others

[6] R. Kinjo, T. Kii, M. Shibata, M. A. Bakr, Y. W. Choi, M. Omer, K. Yoshida, H. Negm, N. Kimura, K. Ishida, H. Imon, T. Komai, K. Shimahashi, H. Zen, T. Sonobe, K. Masuda, K. Nagasaki and H. Ohgaki, "Improvement of trapped field in DyBaCuO bulk by proton irradiation", *Physica C*, Vol. 484 (2013) 117 (refereed).

[7] R. Kinjo, M. A. Bakr, Y.W. Choi, H. Imon, K. Ishida, T. Kii, N. Kimura, K. Komai, K. Masuda, K. Nagasaki, H. Ohgaki, M. Omer, S. Shibata, K. Shimahashi, T. Sonobe, K. Yoshida and H. Zen, "Enhancement of Undulator Field in Bulk HTSC Staggered Array Undulator with Hybrid Configuration", *Proceedings of the 33th International Free Electron Laser Conference 2011*, Jul. 07, 2012.